46th AIAA/ASME/SAE/ASEE Joint Propulsion Conference & Exhibit
25 - 28 July 2010, Nashville, TN

AIAA 2010-6967

Analysis of Interacting, Under-Expanded, Rarefied Jets

Wenhai Li[1] and Foluso Ladeinde.[2]
Department of Mechanical Engineering, Stony Brook University,
Stony Brook, New York, 11794-2300

A numerical study, using the Direct Simulation Monte Carlo (DSMC) approach, of the interaction effects between two identical sonic under-expanded nitrogen jets under rarefied conditions is reported. In this paper, the effects of the jet stagnation Knudsen number (Kn_s), the ratio of the stagnation-to-background pressure (P_s/P_b), and the distance between the jet orifices (L/D) were investigated for a range of these parameters. The background pressure has a very significant effect on the physics of flow. The value of L/D affects the locations of the Mach disk in both primary and secondary jets. But When P_s/P_b is relatively large (such as $P_s/P_b=220$) and L/D is relatively small ($L/D\leq 6.0$), the separation distance L/D has only a mild effect on the location of the Mach disk in the secondary jet. A study of the rotational-translational non-equilibrium showed that large deviations between the translational and rotational temperatures can be found in the secondary jet, especially in the vicinity of the orifice plate.

Nomenclature

D	=	diameter of orifice
D_M	=	diameter of Mach disk
d	=	diameter of gas molecule
$f(\theta)$	=	angular distribution function
Kn	=	Knudsen number
Kn_p	=	penetration Knudsen number
k	=	Boltzmann constant
M	=	Mach number
m	=	mass of gas molecule
N	=	number of particles
n	=	number density
P	=	pressure
Re	=	Reynolds number
R	=	gas constant; radial length
T	=	temperature
u	=	velocity
X_M	=	horizontal distance from orifice exit to Mach disk
Z_r	=	rotational collision number
γ	=	specific heat ratio
θ	=	interaction angle
λ	=	mean free path
ξ	=	rarefaction parameter

Subscripts

b	=	value of background gas

[1] Graduate Research Assistant
[2] Life Member and Associate Fellow of AIAA

Copyright © 2010 by the American Institute of Aeronautics and Astronautics, Inc. All rights reserved.

r = value of rotational mode
s = value at stagnation conditions
t = value of translational mode

I. Introduction

THE The interaction between rarefied free jets has received some attention in recent years because of the relevance to rockets and other space vehicles.[1-4] For rockets, two or more nozzles are used in order to provide a large impulse and stability. Because of the high altitude, the pressure is low, which causes the plumes from each nozzle to have a large radial extent. Therefore, an interaction between the neighboring plumes may occur. Another example is the spacecraft's Orbiter Reaction Control System (RCS),[5-7] which always comprises of many primary and vernier engines. The RCS can provide the thrust for altitude maneuvers and for small velocity changes along the orbiter axis by firing selected engines. If adjacent engines are fired simultaneously, an interaction between the two jets can occur. The jet interaction phenomena can also be seen in the satellite's Altitude Control System (ACS),[8] which is used to control the altitude of a satellite. This system is generally formed by an array of small thrusters. Because the size of the satellite is small and the plume size is large in high altitude, jet interaction between the adjacent plumes can be observed. Recently, the interaction of multiple plumes has become more and more important with the development of microspacecraft.[9] Many designs of micro-propulsion systems involve the use of thruster arrays for orbital maneuvers, such as attitude control and orbit rising. The thruster arrays can be batch-fabricated using Microelectromechanical Systems (MEMS) techniques. The thruster array can increase the flexibility for microspacecraft since thrusters can be fired in specific sequences, or simultaneously, to obtain desired impulse profile and thrust level for a particular maneuver. In thruster array, the distance between the thrusters is always very small. Therefore, the interaction between the plumes may occur. Another popular application of the interacting jets is in the plasma-aided materials processing technique.[10] A particular example is expanding thermal plasma (ETP) thin film decomposition, which can deposit thin films or coating on the materials. Schaepkens[11] has found that in the ETP process, a properly optimized dual-source system can deposit a uniform thick coating of abrasion-resistant material across a width of 30 cm of substrate in one pass. Autric[12] also reported experimental data on the dual-source crossed beams pulsed laser deposition technique for the production of cryolite thin films.

The interaction between the jets can have several effects on spacecraft operation, such as changes in the thrust impulse profile, the dynamic of jet impingement, the heat flux and pressure force on the spacecraft surfaces, the contamination, stability performance, and noise generation.[13,14] These phenomena can cause a lot of difficulties in the design of a spacecraft. For example, when the interaction effects are strong, there is a backflow region generated in the interaction region.[15] The backscattered molecules can enhance contamination and can also lead to relatively high heat flux and surface forces that exceed the fatigue failure limit for metallic aircraft structures. Another example is for acoustic generation. It was observed that, for multiple interacting jets, it has advantage for the noise reduction.[16-18]

Rapidly expanding plumes at high altitudes involve the entire range of the flow regimes, from continuum flows near the nozzle exit to transitional and the free molecular flows at large distances from the nozzle. Furthermore, for flight at different altitudes, the plumes from the spacecraft exhaust may be expanded into a background with finite pressure for the flight in the earth's atmosphere, or into vacuum for flight in outer space. Therefore, the rarefaction effects could become an important issue for the multiple jet interaction. If the jets are expanding into vacuum, only the interactions between the molecules of the two jets need be considered. If the interaction effect is strong, strong oblique shocks wave are formed, as shown in Figure 1(a). The interaction region, which is surrounded by the oblique shocks, looks like another jet plume and will be referred to as the secondary jet. If the jets are expanding into a background with finite pressure, the interactions between the molecules of the jets with the background flows become important. If the interaction is strong, barrel shocks and jet boundaries, which take on concave curvature, are formed. Together with the normal shock waves (Mach disks, for both primary and secondary jets) and the oblique shocks, well-known 'primary-secondary' shock-cell structures are formed (Figure 1(b)).

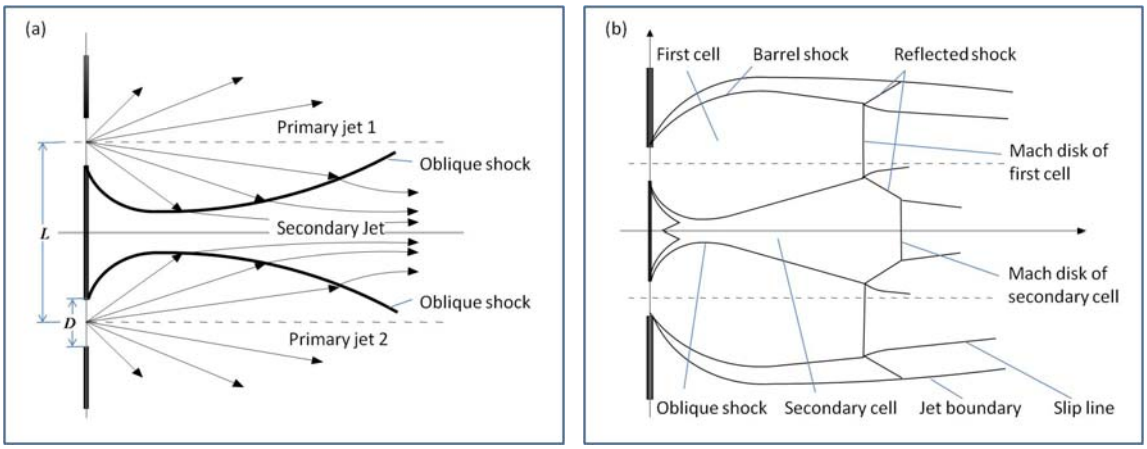

Figure 1. Shock structure of dual interacting jets: (a) expanding into vacuum; (b) expanding into a background with finite pressure

Experimental investigation of high speed jet flows is expensive and involves practical difficulties, such as the need for non-intrusive flow measurements at high speed. Thus, only a few of experimental studies are available.[19, 20] Therefore, numerical analysis becomes a very attractive option. For the flow in the rarefied regime, the DSMC method has proven to be a powerful technique and many researchers[21, 22] have used the method for the dual interacting jets expanding into vacuum, such as Zhu and Dagum,[5-7] Ketsdever,[9] and Wu.[23] The numerical investigation of jets expanding into a background with finite pressure is extremely challenging for numerical methods, including the DSMC approach. The density in the flow field is much higher than that for jets expanding into vacuum. Therefore, more simulated particles are needed. Since the problem is fully three-dimensional, the computation is very expensive. Also, the implementations of the downstream boundary conditions, where background pressure and temperature are specified, pose additional difficulties for the DSMC method. The traditional method, which usually includes a large pressure reservoir in the computation, is very expensive. Recently, the "particle conservation" method was developed,[24-26] to address this problem. With the flow velocity calculated at the downstream boundary and background pressure and temperature specified, correct stream boundary conditions can be directly applied in DSMC without using pressure reservoir. The method has been successfully used in single under-expanded jet calculations by Wu[27] and the author,[28] but not for interacting rarefied jets. Usami[29] numerically simulated dual interacting jets expanding into a region with finite pressure by using DSMC and successfully captured the 'primary-secondary' shock-cell structures. However, the detailed analysis of the interacting effects was not investigated.

A more detailed investigation of the interaction between nitrogen jets under rarefied conditions is undertaken for both cases when the background region is either vacuum or with finite pressure. In specifics, the response of the system to various combinations of the jet stagnation Knudsen number Kn_s, the under-expanded jet pressure ratio P_s/P_b, and the separation between the two orifices L/D, is investigated with a focus on the shock structures and the thermal non-equilibrium behaviors. A DSMC code developed for this purpose is first validated for the related problem of single under-expanded jet. It is then applied to the interacting jets, without modifications, within $0.002 \le Kn_s \le 0.02$, $1.5 \le L/D \le 8.0$, and P_s/P_b values between 50 and values that approach infinity.

II. The Numerical Method and Its Validation

A parallel, three-dimensional direct simulation Monte Carlo (DSMC) program has been developed for the present study, using procedure similar to those in Bird.[30] A review of the advances in the DSMC method in fluid mechanics has been presented by Oran et al.[31] The method solves the Boltzmann equation by using simulated particles to statistically model the molecular motions and intermolecular collisions in real gas flows. Since the Boltzmann equation governs all flow regimes, the DSMC method is theoretically applicable to the simulation of gas flows in all regimes (continuum, rarefied, and transition). In the current implementation, the "variable soft sphere"

(VSS) molecular model[30] is used, with Bird's "no time counter" (NTC) algorithm[30] for the collision mechanics. At every time step, molecular motion and intermolecular collision calculations are decoupled, which requires that the time step size be smaller than the mean molecular collision interval. Since the statistical error associated with the procedure is inversely proportional to the square root of sampling size,[30] calculations are expensive for small Knudsen number flows. Three dimensional models, such as the ones in this study, make the situation even worse. Improved computational performance can be obtained through parallel execution, to which the DSMC algorithm is readily adaptable through domain decomposition.

The Borgnakke-Larsen phenomenological model[30] is used for the rotational-translational (RT) relaxation process in this investigation, whereby, the rotational relaxation is quantified in terms of a characteristic rotational collision number Z_r, which is approximately the reciprocal of the number of collisions required to reach equilibrium between the translational energy and rotational energy. The relaxation process is governed by Jean's equation:[30]

$$\frac{DT_r}{Dt} = \frac{T_e - T_r}{\tau_r} = \frac{T_e - T_r}{\tau \cdot Z_r} \quad , \tag{1}$$

where T_e is the equilibrium temperature, τ is the collision time, and $\tau_r = \tau \cdot Z_r$ is the rotational relaxation time. Although this phenomenological model is not able to resolve the correct distribution function of rotational energy in cases of non-maxwellian distribution, it has been shown to provide reasonable macroscopic values of T_r.[32] Moreover, vibrational relaxation could be neglected in this study.

The implementation of the downstream boundary conditions is a very important task in the simulation and the present approach follows the "particle conservation" procedure in Wu.[26] Here, an implicit iterative scheme is used to introduce the background particles entering into the flow region at the boundaries between the background and the region of the flow. In this procedure, then mean velocity, u_e, and the average number of particles leaving the computational domain, N_+, are first obtained from the calculations in the previous time step for each boundary cell "m" (Figure 2). Then, the number of particles N_- entering each boundary cell in the current time step is calculated by applying the conservation of particle fluxes under the specified pressure and temperature boundary conditions:

$$\left(u_e\right)_m^t = \frac{N_+^{t-\Delta t} - N_-^t}{n_b A} \quad , \tag{2}$$

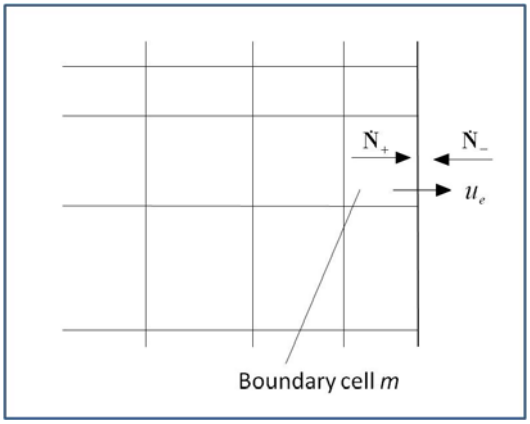

Figure 2. Illustration of the "particle conservation" method

where A is the area on a downstream boundary cell, and the downstream number density n_b is calculated as $n_b = P_b/(kT_b)$, where P_b and T_b are the pressure and temperature at the downstream boundaries. Thus, for each boundary cell, the particles entering the flow region from the background are introduced by sampling from a Maxwellian distribution with the calculated mean flow velocity u_e and the background temperature T_b. Although Cai and Boyd[33] argued that this method could cause statistical error in the flow field, the method has been successfully used for the simulation of single under-expanded jet.[27, 28] In this study, to further reduce any statistical error from this method, the calculated mean flow velocities in the boundary cells are averaged over time.

Several problems have been used to validate the developed DSMC code prior to its use for the interacting jet investigation. One of these involves a single sonic under-expanded nitrogen jet, issuing into a three dimensional rectangular chamber at specified background pressure and density. The stagnation pressure (P_s) and temperature (T_s) of the jet are *30* torr and *293* K, respectively. Several values of stagnation-to-background pressure ratios (P_s/P_b)

between *10* and value approaches infinity are investigated while the background temperature (T_b) is set to the source stagnation temperature. Each case runs for three different values of the stagnation Knudsen number (Kn_s) of *0.05*, *0.005*, and *0.002*. The geometry of the simulated region is shown in Figure 3. Only one quarter of the domain is simulated on the assumption of symmetry. The jet flow exhausts through a circular orifice located at the x=0 plane. The boundary conditions are set as follows:

(1) Symmetry boundary conditions are imposed on both the $y=0$ and $z=0$ planes;

(2) For the $x=0$ plane, sonic conditions are used for the particles entering through the orifice and the orifice plate is set to be a fully diffusive wall with a temperature equal to the background temperature;

(3) The background pressure P_b and temperature T_b are specified for all outflow boundaries.

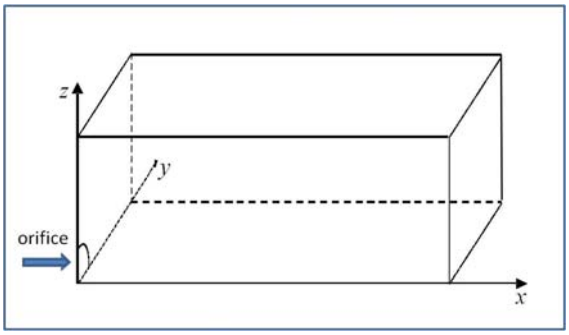

Figure 3.The computational domain for the DSMC calculation of under-expanded jets in this paper, showing a quarter of the full domain, assuming symmetry

Note that, to correctly specify the downstream boundary conditions, the size of the computational domain needs to be sufficiently large so that the influence of the jet plume is neglectable at the downstream boundaries. The detailed simulation parameters are given in Table 1. The DSMC simulations are carried out in parallel, using the Message Passing Interface (MPI) protocol. Figure 4 shows the typical grid configurations for the DSMC calculations. Note that to achieve good load balance, automatic domain decomposition is used to allocate an equal number of particles to each sub-domain.

Case	Kn_s	P_s/P_b	CPUs	Nozzle Diameter (m)	ξ ($\frac{dynes}{cm \cdot K}$)	Size of Domain	Particle Weight	No. of Particles	No. of Cells
1	0.05	∞	16	2.73957×10^{-5}	0.0000	$25D \times 6D \times 6D$	1.302×10^{4}	4, 149, 620	484, 652
2	0.05	200	16	2.73957×10^{-5}	0.0253	$25D \times 6D \times 6D$	2.170×10^{4}	6, 465, 380	542, 346
3	0.05	100	16	2.73957×10^{-5}	0.0357	$25D \times 6D \times 6D$	4.894×10^{4}	8, 787, 720	605, 248
4	0.05	50	16	2.73957×10^{-5}	0.0505	$20D \times 6D \times 6D$	8.684×10^{4}	10, 450, 762	663, 736
5	0.05	20	16	2.73957×10^{-5}	0.0799	$18D \times 5D \times 5D$	2.605×10^{5}	14, 256, 128	727, 352
6	0.05	10	36	2.73957×10^{-5}	0.1130	$16D \times 4D \times 4D$	8.075×10^{5}	15, 502, 532	730, 856
7	0.005	∞	36	2.73957×10^{-4}	0.0000	$25D \times 6D \times 6D$	8.680×10^{5}	17, 443, 800	758, 426
8	0.005	200	36	2.73957×10^{-4}	0.2527	$25D \times 6D \times 6D$	1.736×10^{6}	20, 201, 509	841, 730
9	0.005	100	36	2.73957×10^{-4}	0.3574	$25D \times 6D \times 6D$	8.681×10^{6}	17, 818, 486	809, 932
10	0.005	50	36	2.73957×10^{-4}	0.5055	$20D \times 6D \times 6D$	8.681×10^{6}	35, 391, 399	1, 608, 670
11	0.005	20	36	2.73957×10^{-4}	0.7922	$18D \times 5D \times 5D$	2.171×10^{7}	34, 868, 988	2, 328, 034
12	0.005	10	36	2.73957×10^{-4}	1.1303	$16D \times 4D \times 4D$	5.208×10^{7}	29, 293, 616	3, 661, 702
13	0.002	∞	36	6.83991×10^{-4}	0.0000	$25D \times 6D \times 6D$	1.953×10^{7}	12, 124, 814	1, 348, 216
14	0.002	200	36	6.83991×10^{-4}	0.6318	$25D \times 6D \times 6D$	6.510×10^{7}	25, 142, 704	2, 285, 702
15	0.002	100	36	6.83991×10^{-4}	0.8935	$25D \times 6D \times 6D$	9.766×10^{7}	32, 296, 781	2, 691, 398
16	0.002	50	36	6.83991×10^{-4}	1.2637	$20D \times 6D \times 6D$	5.208×10^{7}	93, 928, 219	6, 261, 882
17	0.002	20	36	6.83991×10^{-4}	1.9980	$18D \times 5D \times 5D$	1.563×10^{8}	78, 154, 987	5, 086, 774
18	0.002	10	36	6.83991×10^{-4}	2.8256	$16D \times 4D \times 4D$	4.688×10^{8}	84, 988, 055	6, 537, 548

Table 1. Simulation conditions for DSMC simulation of single under-expanded jets ($P_s=30$ torr and $T_s=298$ K).

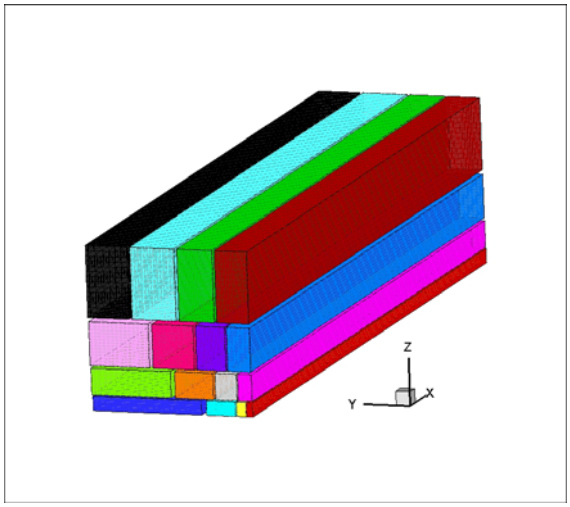

Figure 4. A typical grid for the DSMC simulation running on *16* CPUs

A. Expansion into Vacuum

For free jet expanding into vacuum ($P_s/P_b \to \infty$) from a sonic orifice, the only flow parameter is the jet stagnation Knudsen number Kn_s, which is also related to the Reynolds number at the orifice exit, Re_D^*:

$$Kn_s = \frac{\lambda_s}{D} = \frac{k}{\sqrt{2}\pi d^2} \cdot \frac{T_s}{P_s D} = \frac{1}{\mathrm{Re}_D^*} \sqrt{\frac{\pi\gamma}{2}} \cdot \left(\frac{2}{\gamma+1} \right)^{\frac{1}{\gamma-1}} . \tag{3}$$

Therefore, for a free jet expanding into vacuum at a fixed temperature T_s, Kn_s (Re_D^*) is determined only by the product of P_s and D. This quantity (P_sD), with units of torr×mm, is frequently used in experiments to characterize sonic jet expansion. Marrone[34] and Mori[35] experimentally measured the centerline properties of free jet for the case where $P_sD=15$ torr×mm ($Kn_s=2.736\times10^{-3}$), which provides validation data for the present effort (Figures 5 to 8).

In Figure 5, the density contours from the developed DSMC code and from AEROFLO[36] on the $Z=0$ symmetry plane for $P_sD=15$ torr·mm are compared. Excellent agreement is evident. AEROFLO is a compressible Navier-Stokes based multidisciplinary CFD code that is based on high-order discretization in space and time.

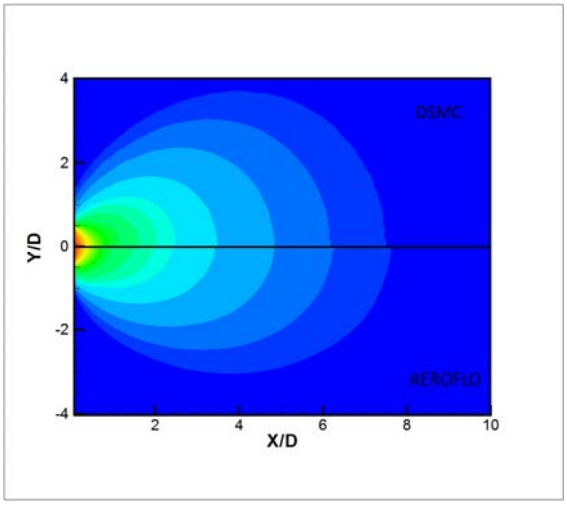

Figure 5. Density contour map on the *Z=0* symmetry plane for the jet ($P_s/P_b \to \infty$, $P_sD=15$ torr·mm) from the present DSMC calculation and from DSMC

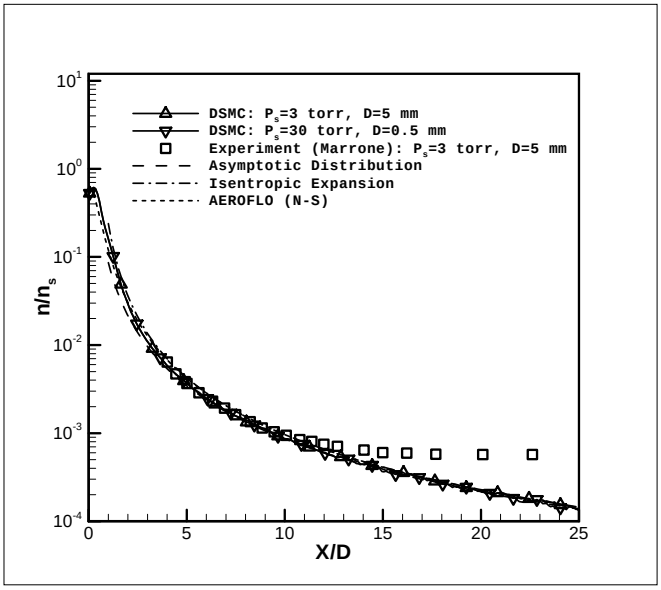

Figure 6. Comparison of calculated and measured density distribution along the centerline. The data comes from Marrone's[34] experiments and continuum calculation from AEROFLO. Also shown are the DSMC results, the asymptotic distribution (Eqn. (4)), and the isentropic expansion relation (Eqn.(6)). Two DSMC results with different flow conditions are shown.

In Figure 6, the density distribution along the jet centerline calculated with the DSMC code is compared with Marrone's experimental data, an asymptotic relation, the isentropic relation, and the result from AEROFLO. Here, the asymptotic relation was developed for this case by several researchers:[37-39]

$$\frac{n}{n_s} = A\left(\frac{D/2}{R}\right)^2 \cdot f(\theta) \ , \tag{4}$$

where R is the radial distance from the orifice and $f(\theta)$ is the angular distribution function, which has the form

$$f(\theta) = \cos^2\left(\frac{\pi}{2}\cdot\frac{\theta}{\theta_{\max}}\right) , \tag{5}$$

where A and θ_{max} are γ-dependent constants. For $\gamma=1.4$, $A=0.345$ and $\theta_{max}=95.2°$.[15] The isentropic relation can also be calculated by

$$\frac{\rho}{\rho_s} = \frac{n}{n_s} = \left(1+\frac{\gamma-1}{2}M^2\right)^{\frac{1}{\gamma-1}} \ , \tag{6}$$

where M is the Mach number distribution within the expansion core, which has an approximation expression of the form:[40]

$$M = (2.2)^{\frac{\gamma-1}{2}}\left[\gamma(\gamma-1)\right]^{\frac{\gamma-1}{4}}\left(\frac{\gamma+1}{\gamma-1}\right)^{\frac{\gamma+1}{4}}(X/D)^{\gamma-1} \ . \tag{7}$$

Two DSMC calculations are shown: (a) $P_s=3$ torr, $D=5$ mm; and (b) $P_s=30$ torr, $D=0.5$ mm. According to the simple theory discussed earlier in this paper, these two calculations should give essentially the same results because the product P_sD is the same. We can see in Figure 6 that this is indeed the case. However, the Navier-Stokes simulations as well as the asymptotic distribution and the isentropic relation give the same density profile. The experimental data also agrees with these results for $X/D\leq12$, with deviations further downstream. We believe the

deviations are due to the inability to obtain perfect vacuum conditions in the experiment, whereas the various calculations had no difficulties enforcing an infinite value for P_s/P_b. Note, however, that the magnitude of the error in the measurement is exaggerated in Figure 6 because of the use of log scale.

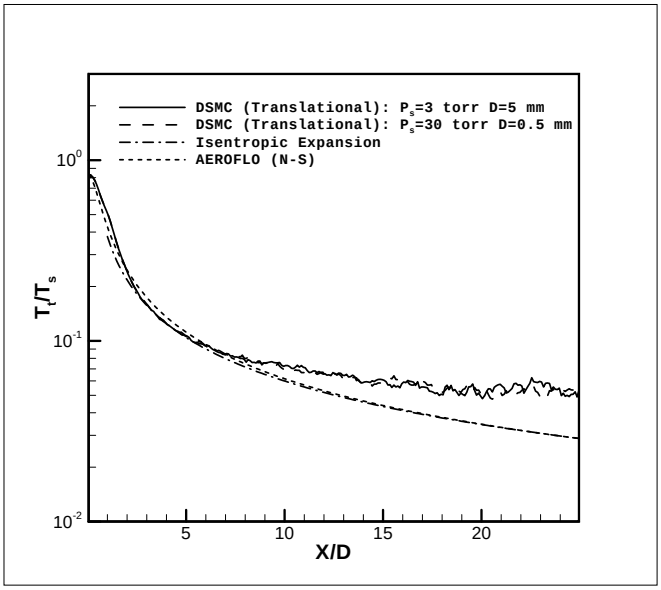

Figure 7. Comparison of translational temperature distribution along the centerline from DSMC simulation and continuum calculation using AEROFLO. The isentropic expansion relation is also shown, as are DSMC results with different flow conditions.

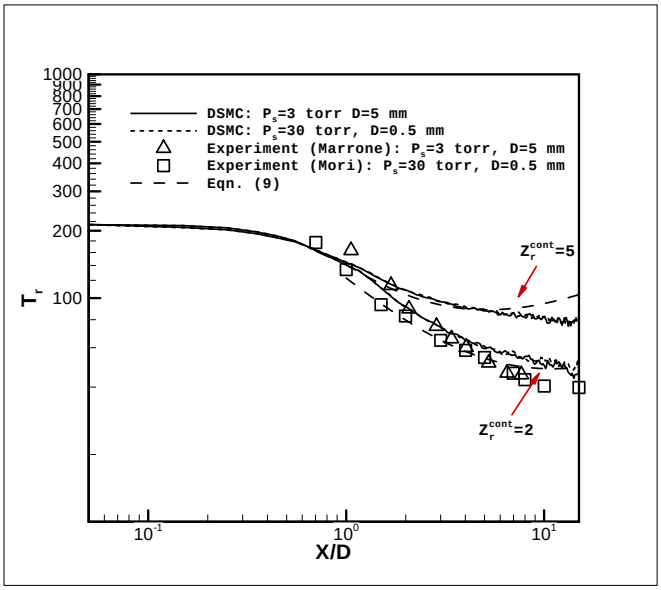

Figure 8. Comparison of calculated DSMC rotational temperature distribution along the centerline with Marrone[34] and Mori's[35] experimental data, and the derived simple rotational temperature decay model (Eqn. (8)). Note that both DSMC and Eqn. (8) are calculated for $Z_r=2$ and $Z_r=5$.

Figure 7 compares the DSMC results for translational temperature with the Navier-Stokes calculations and the isentropic relations, both of which are based on the continuum hypothesis. We see that the two DSMC calculations with different P_s and D values but with the same values of P_sD give identical results. We also observe that the continuum calculations (AEROFLO and isentropic relation) give progressively poorer results as X/D increases, due to increasing non-equilibrium effects downstream.

In Figure 8, the DSMC results for the rotational temperature distribution along the jet centerline are compared with the experimental data from Marrone[34] and Mori.[35] In this plot, an approximate relation:

$$T_r = 0.378318 \times T_s \times (X/D)^{-0.8} + 7.096326 \times (X/D)^{0.408} \times Z_r \,. \tag{8}$$

developed in a previous work by the author,[28] is also shown. Both DSMC calculations and Equation (8) are carried out for $Z_r=2$ and 5, and good agreement with the experimental results is evident for $Z_r=2$, which is a reasonable value for Z_r since the flow temperature drops rapidly and $T \leq 100$ K when $X/D>1$.

B. Expansion into a Region with Finite Pressure

Rather than expanding into vacuum, more complicated flow structures are formed when a jet flows into a region with finite pressure. When the flow is in the continuum regime, the plume expands around the orifice exit to form an inertia-dominated region of high Mach number isentropic flow, which is sometimes called expansion core. Due to the strong interaction between the jet and the background gas, a normal shock wave (Mach disk) and barrel shocks, which take on a concave curvature, are formed. This "shock-cell" structure is shown in Figure 9.

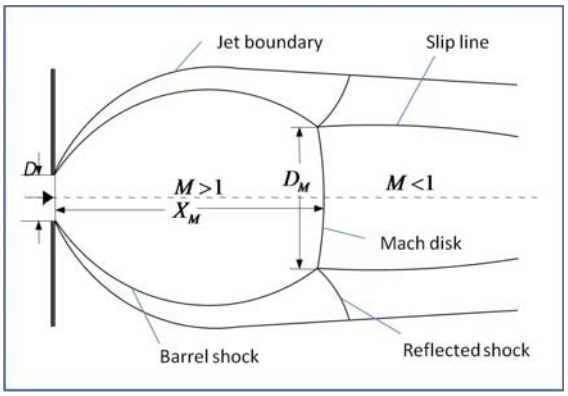

Figure 9. The shock structure from an inviscid under-expanded jet issuing from a sonic orifice

The interaction between the jet molecules and the background gas were studied for single under-expanded jet by Muntz.[41] A rarefaction parameter ξ was proposed as[41]

$$\xi \equiv D(P_s \cdot P_b)^{1/2} / T_s \tag{9}$$

to characterize this interaction. It can be shown that this parameter is inverse proportional to the square root of the pressure ratio P_s/P_b and stagnation Knudsen number Kn_s:

$$\xi = \frac{k}{\sqrt{2}\pi d^2} \cdot \frac{1}{(P_s/P_b)^{1/2} Kn_s} = \frac{k}{\sqrt{2}\pi d^2} \cdot \sqrt{\frac{2}{\pi\gamma}} \cdot \left(\frac{\gamma+1}{2}\right)^{\frac{1}{\gamma-1}} \cdot \frac{\mathrm{Re}_D^*}{(P_s/P_b)^{1/2}} \,. \tag{10}$$

Figures 10 shows the contour maps of the normalized density, translational temperature, rotational temperature, and the Mach number when the under-expanded jet has the parameters $Kn_s=0.002$, $P_s/P_b=50$. Although the flow is rarefied and the shock structure is much dissipated, the "shock-cell" structure can still be observed from these figures. The purpose of these figures is to demonstrate the developed DSMC procedure generates results that are credible based on the known physics of the problem.

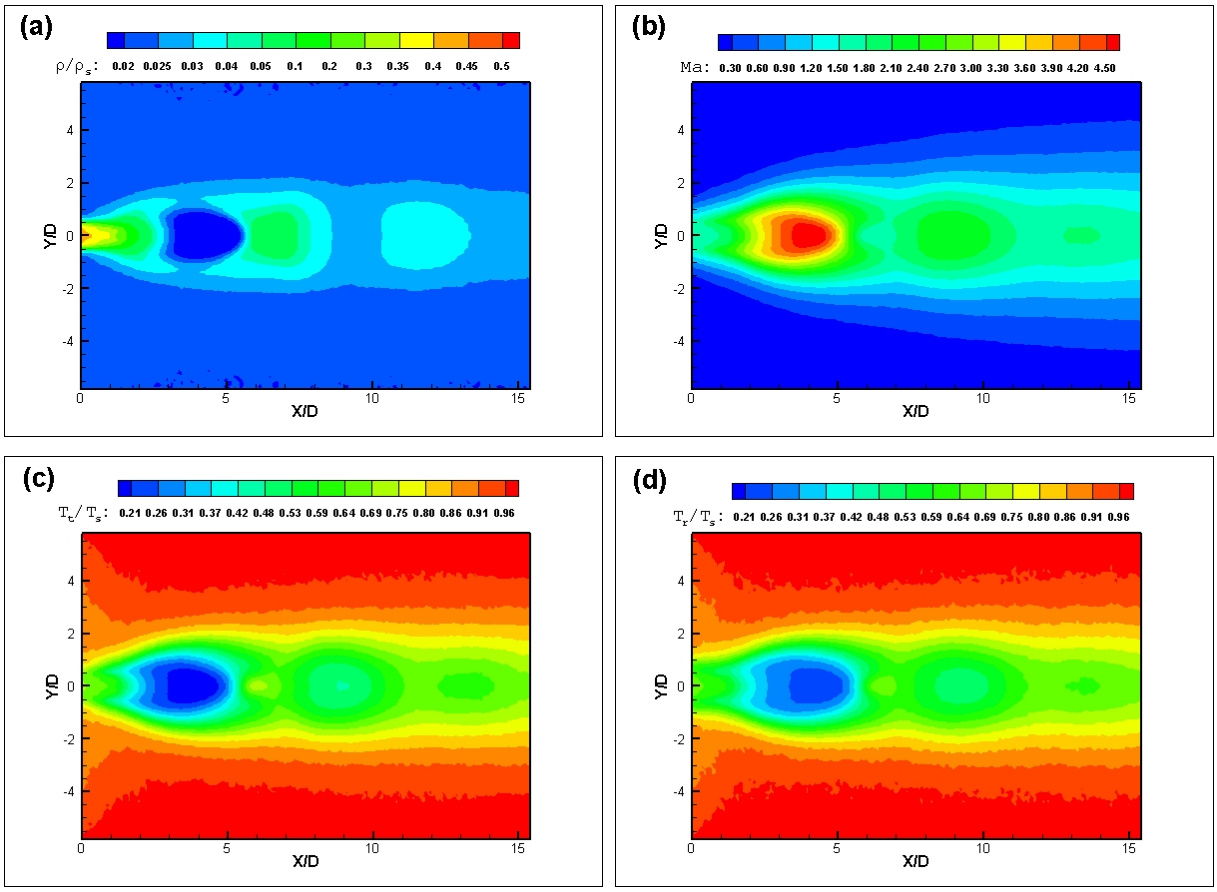

Figure 10. The contour maps of single under-expanded jet at the *Z=0* symmetry plane at Kn_s=0.002, P_s/P_b=50: (a) normalized density; (b) Mach number; (c) normalized translational temperature; (d) normalized rotational temperature.

The location and size of the Mach disk was studied by many researchers. Ashkenas[42] and Crist[43] used the method of electron beam diagnostics to measure the characteristics of Mach disk and proposed empirical correlations for the position and diameter of the disk:

$$X_M / D = 0.67\left(P_s / P_b\right)^{1/2} \tag{11}$$

and

$$D_M / D = 0.24\left(P_s / P_b\right)^{1/2} \quad . \tag{12}$$

Figure 11 shows the location and diameter of the Mach disk predicted by the present DSMC program and the experimental correlations. In the current study, the location of the Mach disk is defined by the position where the local Mach number has the maximum absolute slope. The DSMC results are in good agreement with the experimental correlations.

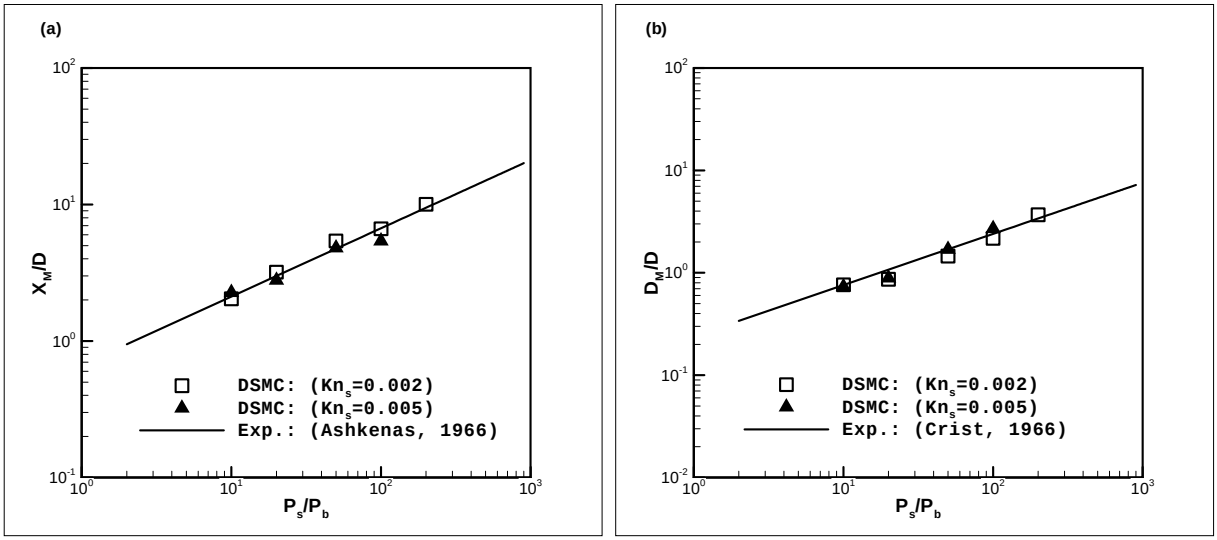

Figure 11. (a) Location and (b) diameter of the Mach disk as a function of pressure ratio, showing agreement between experimental data (Eqns. (11) and (12)) and the present DSMC calculations.

III. Investigation of Interacting Jets

The physics of dual, interacting jets were investigated with the DSMC procedure after establishing the accuracy of the numerical approach for the current type of problems. The physical problem of interest is as in Figure 1, with the computational domain in Figure 12. With the assumption of symmetry, only a quarter of the three-dimensional model is simulated. The flow field is very similar to the one used for the single under-expanded jet except the fact that the orifice is now located at (*0,0,L/2*). The settings of the boundary conditions are also same with those used for single under-expanded jets. The range of stagnation Knudsen number Kn_s chosen from study involve as *0.02*, *0.005*, and *0.002*, and the separation between the orifices are within $1.0 \le L/D \le 8.0$. The stagnation-to-background pressure ratios $P_s/P_b=50$, *100*, *200*, and ∞ are used. The domain is chosen to be sufficiently large so that the influence of interacting jets does not reach the downstream boundary. The stagnation pressure and temperature of the jet flow are $P_s=870$ Pa and $T_s=285$ K, respectively. The detailed simulation parameters for some typical cases are given in Table 2.

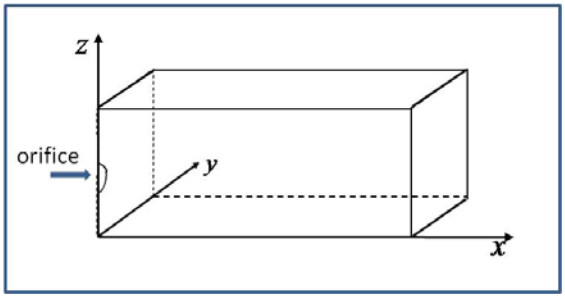

Figure 12. Computational model for the DSMC calculation of interacting jets

A. Expansion into Vacuum

The interaction between the molecules of the two jets was first studied by Dankert and Koppenwallner.[8, 15] They introduced a parameter Kn_p, which is called Penetration Knudsen number, to describe the interaction:

$$Kn_p \equiv \frac{\lambda_p}{l_{ref}} \ , \tag{13}$$

where λ_p is the mean free path of one plume molecules moving through another plume flow field and l_{ref} represents the characteristic length of the flow, which is chosen as the distance from the symmetry plane to the centerline of the

plume as shown in Figure 13. It can be shown that Kn_p is a function of the jet's stagnation Knudsen number Kn_s, the distance of the orifices to the orifice diameter ratio L/D, and the interaction angle θ, which can be expressed as[8]

$$Kn_p(\theta) = \frac{2\sqrt{2}}{\sqrt{\pi}}\sqrt{1+\frac{1}{\gamma}}\cdot\frac{Kn_s}{A}\cdot\frac{L}{D}\cdot\frac{1}{f(\theta)\sin^2\theta} = \frac{2\sqrt{2}}{\sqrt{\pi}}\sqrt{1+\frac{1}{\gamma}}\cdot\frac{Kn_s}{A}\cdot\frac{L}{D}\cdot g(\theta)\ , \tag{14}$$

where

$$g(\theta) = \left[\cos^2\left(\frac{\pi}{2}\cdot\frac{\theta}{\theta_{\max}}\right)\sin^2\theta\right]^{-1}\ , \tag{15}$$

where A and θ_{max} have been defined previously (Equations (4) and (5)). The interaction between the two jets can be characterized by $Kn_{p,min}$, which is the value of Kn_p when $g(\theta)$ attains its lowest value ($\theta \approx 39°$).

Case	Kn_s	P_s/P_b	L/D	Nozzle Diameter (m)	ξ ($\frac{dynes}{cm\cdot K}$)	$Kn_{p,\min}$	Size of Domain	No. of Particles
1	0. 002	220	1. 0	3. 0 × 10^{-3}	0. 6024	0. 0478	35D × 7D × 8D	27, 962, 359
2	0. 002	220	2. 0	3. 0 × 10^{-3}	0. 6024	0. 0956	35D × 7D × 8D	28, 315, 263
3	0. 002	220	3. 0	3. 0 × 10^{-3}	0. 6024	0. 1434	35D × 6D × 8D	25, 651, 298
4	0. 002	220	6. 0	3. 0 × 10^{-3}	0. 6024	0. 2867	30D × 6D × 9D	20, 395, 871
5	0. 002	220	8. 0	3. 0 × 10^{-3}	0. 6024	0. 3823	30D × 5D × 10D	21, 745, 141
6	0. 005	∞	3. 0	3. 0 × 10^{-3}	0. 0000	0. 3584	35D × 6D × 8D	12, 104, 632
7	0. 005	200	3. 0	1. 18908 × 10^{-3}	0. 2527	0. 3584	35D × 6D × 8D	20, 194, 251
8	0. 005	100	3. 0	1. 18908 × 10^{-3}	0. 3574	0. 3584	30D × 6D × 8D	22, 325, 751
9	0. 005	50	3. 0	1. 18908 × 10^{-3}	0. 5055	0. 3584	30D × 6D × 6D	21, 146, 486
10	0. 02	∞	3. 0	1. 18908 × 10^{-3}	0. 0000	1. 4336	30D × 6D × 8D	6, 372, 875
11	0. 02	200	3. 0	3. 0 × 10^{-4}	0. 0632	1. 4336	25D × 6D × 8D	10, 325, 459
12	0. 02	100	3. 0	3. 0 × 10^{-4}	0. 0894	1. 4336	25D × 6D × 8D	10, 698, 869
13	0. 02	50	3. 0	3. 0 × 10^{-4}	0. 1264	1. 4336	25D × 6D × 8D	12, 326, 652

Table 2. Simulation conditions for DSMC simulation of interacting jets

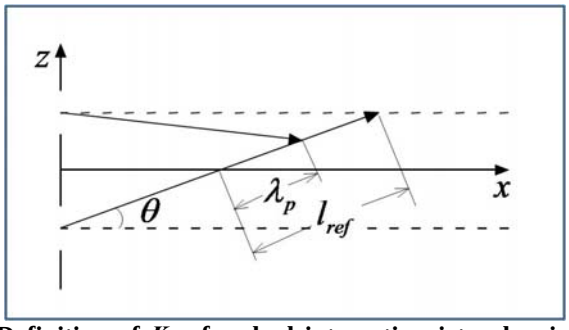

Figure 13. Definition of Kn_p for dual interacting jets, showing the penetration mean free path λ_p, the reference length l_{ref}, and the interaction angle θ.

Figures 14 and 15 show the contour maps of the normalized density, translational temperature and rotational temperature on the $y=0$ and $z=0$ symmetry planes for $Kn_s=0.003$, $L/D=3$, and $P_s/P_b\rightarrow\infty$. In this case, the interaction between the two jets is strong and we can clearly observe an interaction region that is formed. From the temperature contours, it is clear that the secondary jet has higher enthalpy than the primary jets. This is due to the fact that in the secondary jet, the collisions between the molecules of the two jets nullify the z-velocity component of the molecules. Therefore, the kinetic energy is converted into thermal energy. Figure 15 shows that the secondary jet expands at a faster rate in the y-direction. Compare the translational and rotational temperatures contours; it can be observed that the differences between the translational and rotational temperatures are significant in the secondary jet, especially when x/D is small. We also can observe that the maximum points for the density and temperature profiles on the x-axis are not at the same position. In this case, the density has a maximum value at $x/D\approx3$, while the translational and rotational temperatures have a maximum value at $x/D\approx1$.

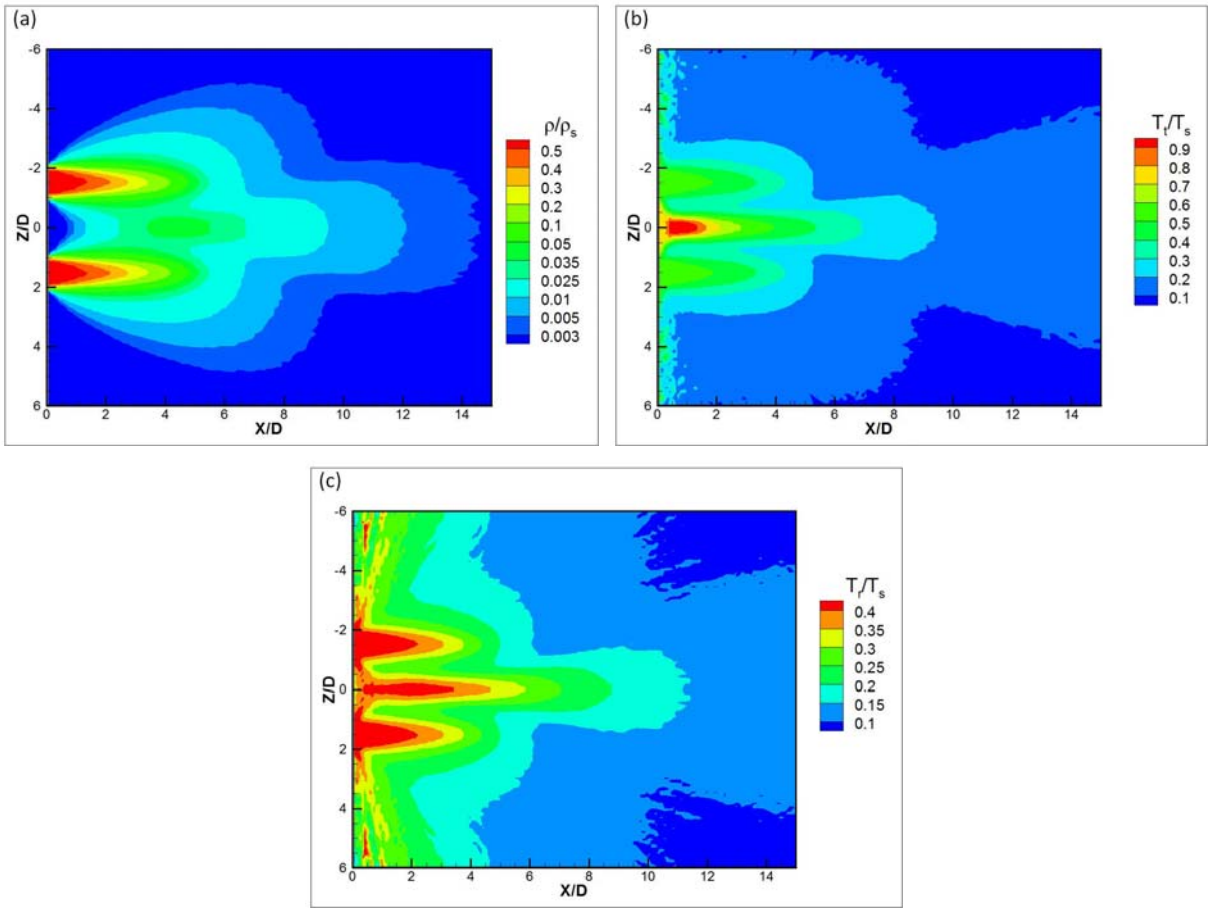

Figure 14. The (a) density; (b) translational temperature; (c) rotational temperature contours on the $y=0$ symmetry plane for $Kn_s=0.003$, $L/D=3$, and $P_s/P_b\rightarrow\infty$.

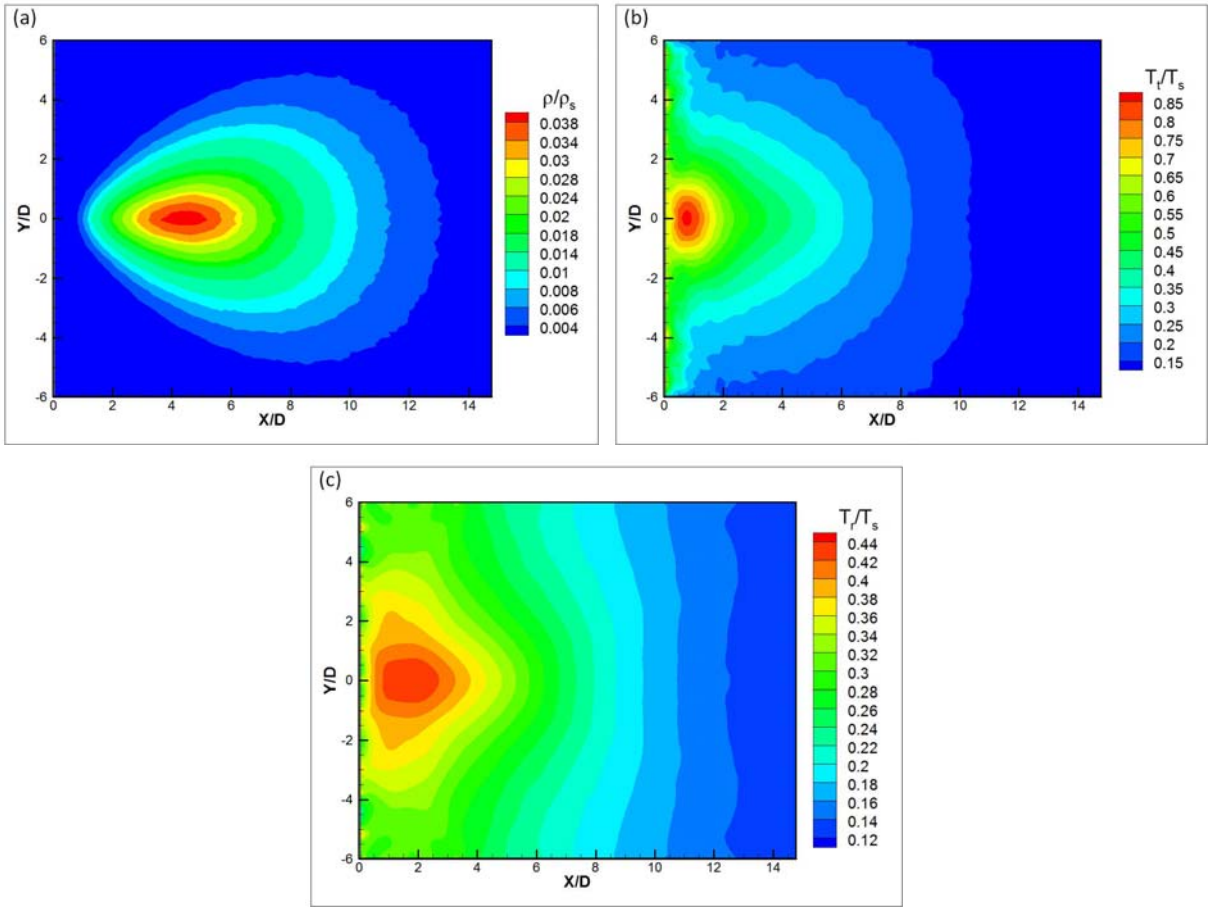

Figure 15. The (a) density; (b) translational temperature; (c) rotational temperature contours on the *z=0* symmetry plane for $Kn_s=0.003$, *L/D=3*, and $P_s/P_b\rightarrow\infty$.

Figures 16 shows the normalized density, translational temperature and rotational temperature contours on the *y=0* symmetry plane for $Kn_s=0.03$, *L/D=3*, and $P_s/P_b\rightarrow\infty$. Compared with Figure 14, the flow is more rarefied due to a larger Kn_s value. In this case, the secondary jet is hard to found in the density contour, while it is still can be observed in temperature contours. Therefore, compared to the density field, the flow temperatures are more sensitive to the interaction between the two jets. Also, because the flow is very rarefied, although the translational temperature in the secondary jet is higher than those in the primary jets, it can be found that the rotational temperature in the secondary jet is much smaller.

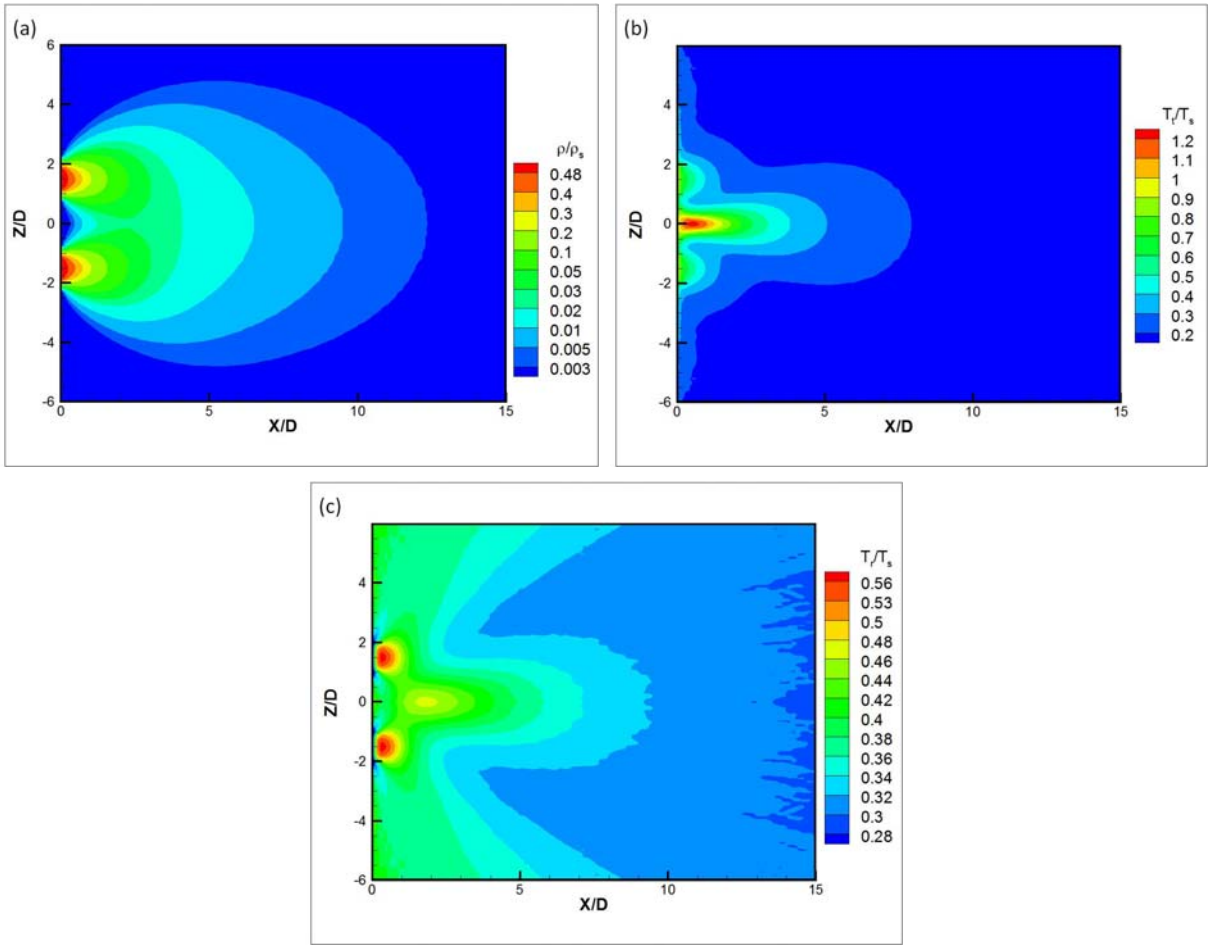

Figure 16. The (a) density; (b) translational temperature; (c) rotational temperature contours on the *y=0* symmetry plane for $Kn_s=0.03$, $L/D=3$, and $P_s/P_b\rightarrow\infty$.

B. Expansion into a Region with Finite Pressure

When interacting jets flow into a region with finite pressure, the interactions are those between the jets (Equation (14)) and between the jets and the background gas (Equation (10)). The physics of the problem are thus determined by three parameters Kn_s, L/D, and P_s/P_b. Although interaction between the jet flow and background gas have been carefully studied for single under-expanded jet,[41] those for interacting jets have not received enough attention. The two extreme cases $L/D=0$ and $L/D=\infty$ are of interests. When $L/D=0$, the flow is identical to that of a single under-expanded jet with $P_s'=2P_s$, and the rarefaction parameter takes the form $\xi_{primary}'^{-1}=\xi_{secondary}'^{-1}=\sqrt{2}\xi^{-1}$. When $L/D\rightarrow\infty$, the interaction between the two jets can be neglected. Therefore, the rarefaction parameter for the jets take the form $\xi_{primary}'=\xi$ and $\xi_{secondary}'\rightarrow\infty$. To summarize, for the both primary and secondary jet, the interaction between the jet molecules with the background molecules can be classified as

$$\xi' = c\xi\,, \tag{16}$$

where c depends on L/D

$$c_{primary} = \begin{cases} 1/\sqrt{2} & \text{for} \quad L/D = 0 \\ 1 & \text{for} \quad L/D = \infty \end{cases} \tag{17}$$

and

$$c_{secondary} = \begin{cases} 1/\sqrt{2} & \text{for} \quad L/D = 0 \\ \infty & \text{for} \quad L/D = \infty \end{cases}. \tag{18}$$

For single under-expanded jet, the location of the Mach disk only depends on P_s/P_b. For interacting under-expanded jets, the Mach disks exist for both primary jet and secondary jets, and the location of the Mach disks should also be a function of L/D. We can estimate the Mach disk location for both of the primary and secondary jets as

$$X'_M / D = c_M X_M / D\,, \tag{19}$$

where c_M is also a function of L/D which satisfy the conditions:

$$c_{M,primary} = \begin{cases} \sqrt{2} & \text{for} \quad L/D = 0 \\ 1 & \text{for} \quad L/D = \infty \end{cases} \tag{20}$$

and

$$c_{M,secondary} = \begin{cases} \sqrt{2} & \text{for} \quad L/D = 0 \\ 0 & \text{for} \quad L/D = \infty \end{cases}. \tag{21}$$

Soga[19] experimentally measured the density and rotational temperature properties for interacting jets when $Kn_s=0.002$ and $P_s/P_b=220$ for several values of L/D, which provides validation data for the present effort. The details of the conditions are shown in Table 3. Note that two sets of conditions are used for the density and temperature measurement, respectively.

No.	P_s	D	T_S	L/D	Kn_s	P_b	M^*	Purpose	Method
1	*870* Pa	*3* mm	*285* K	0, 1.2, 2, 3, 6, 8, ∞	1.95142×10^{-3}	4.0 Pa	1.0	Density measurement	Electron beam fluorescence
2	*650* Pa				2.61190×10^{-3}	3.1 Pa		Temperature measurement	

Table 3. Details of Soga's experiment[19]

Figure 17 shows the density, translational temperature, and rotational temperature contours at the $y=0$ symmetry plane for $L/D=3$, $Kn_s=0.002$, $L/D=3.0$, and $P_s/P_b=220$. Compared with the results of the jets expanding into vacuum, it can be seen that the existence of the background pressure greatly changes the flow structure. Although much dissipated, the primary and secondary shock cells can still be observed, especially in the temperature contours. Figure 18 shows the same contours but for z=0 symmetry plane, which also shows the shock-cell structure due to the existence of background gas.

Figures 19 shows the density distribution along the $(x,0,0)$ symmetry axis compared with the experimental data. Note that two sets of DSMC results are presented: $P_s/P_b=220$ and $P_s/P_b\rightarrow\infty$. The plot shows very good agreement between the DSMC results and the measurements. The monotonic decay of density for the case $P_s/P_b\rightarrow\infty$ is expected based on the results from the previous section. Figure 20 shows the rotational temperature distribution along the $(x,0,0)$ axis. Close agreement between the calculations and the experimental data is also evident. Note that the experimental data is available only for $X/D<8.0$.

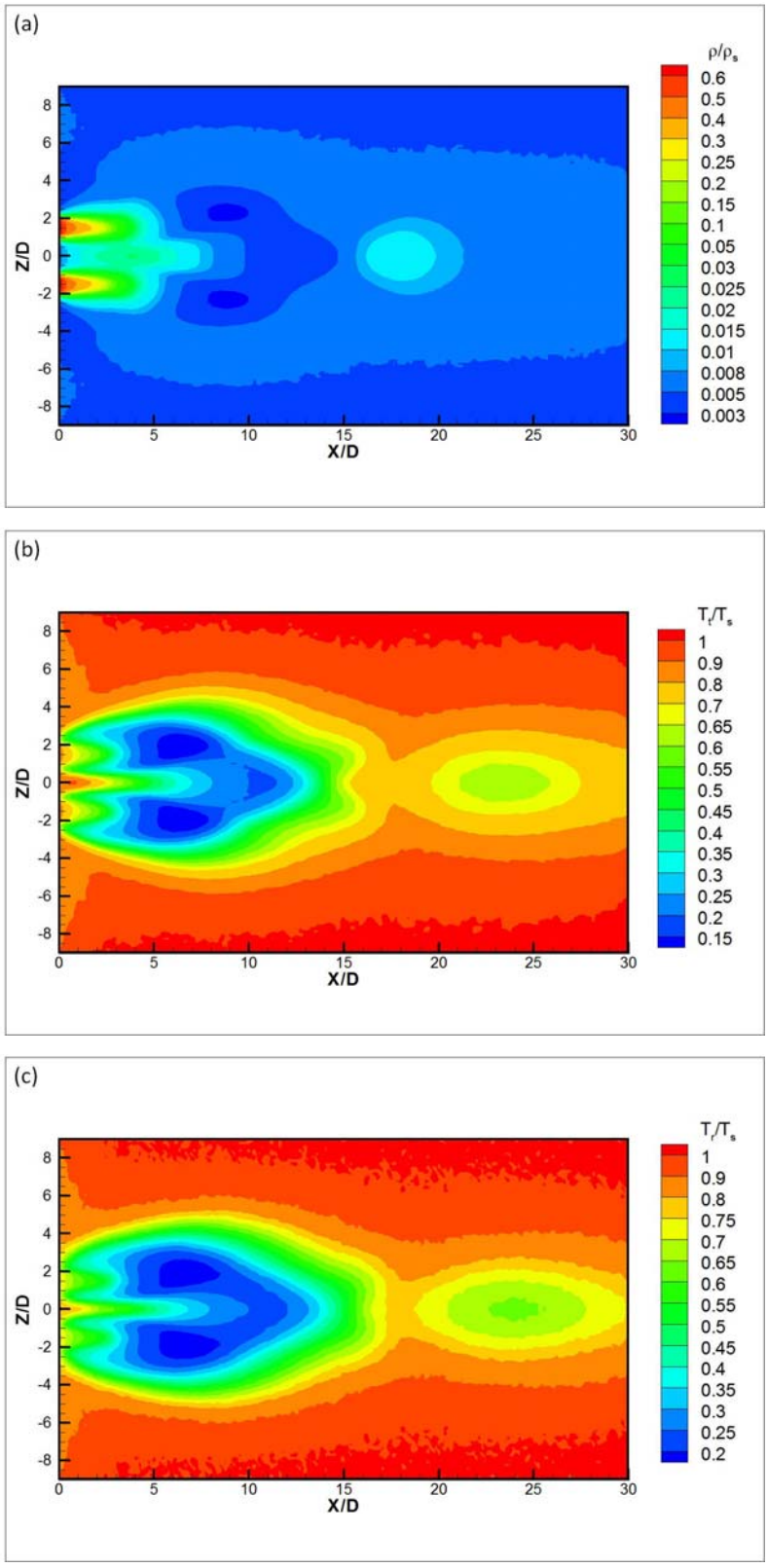

Figure 17. The (a) density; (b) translational temperature; and (c) rotational temperature contours in *y=0* plane for *L/D=3.0*, Kn_s*=0.002*, and P_s/P_b*=220*

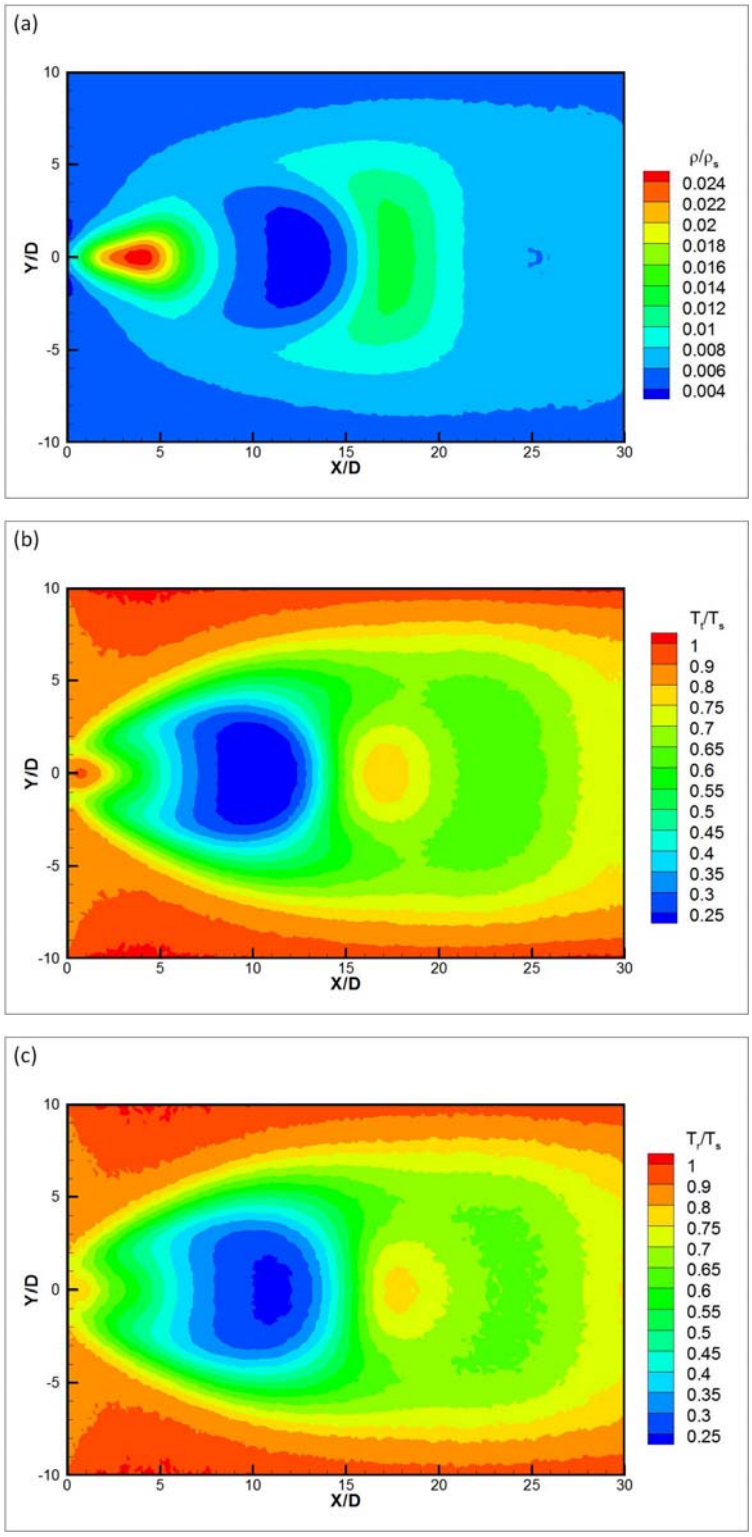

Figure 18. The (a) density; (b) translational temperature; and (c) rotational temperature contours in *z=0* plane for *L/D=3.0*, Kn_s*=0.002*, and P_s/P_b*=220*

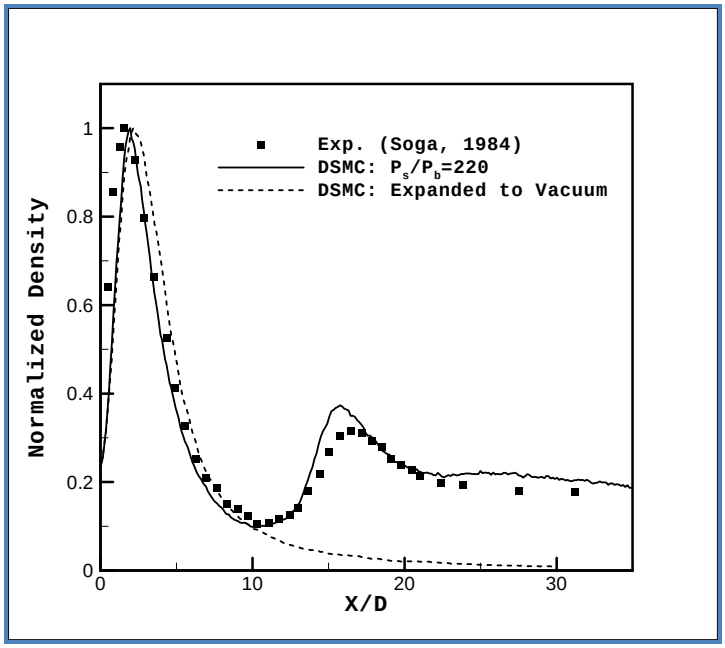

Figure 19. Density distribution along the (*x,0,0*) axis showing comparison with Soga's experimental data[19] for case of *L/D=3.0*, $P_s/P_b=220$, and $Kn_s=0.002$. The case $P_s/P_b\rightarrow\infty$ is shown for the reference of vacuum background.

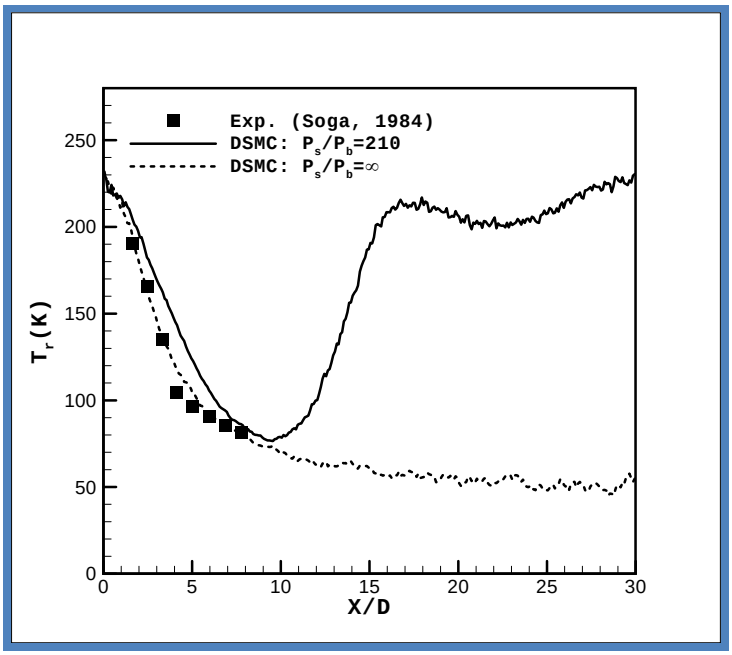

Figure 20. Rotational temperature distribution along the (*x,0,0*) axis showing comparison with Soga's experimental data[19] for case of *L/D=3.0*, $P_s/P_b=210$, and $Kn_s=0.0027$. The case $P_s/P_b\rightarrow\infty$ is shown for the reference of vacuum background.

Figures 21 and 22 show the density, translational temperature, and rotational temperature contours at $y=0$ as in Figure 17, but with different values of L/D (1.5 and 6.0, respectively). Compared with Figure 17, in which $L/D=3.0$, the effects of the separation distance L/D are shown. When $L/D=1.5$ and 3.0, the secondary jet is clearly formed, especially in temperature contours. When L/D is increased to 6.0, the interaction between the two jets is much weaker, as one should expect.

Figure 23 is prepared to further estimate the effect of L/D. The plot shows the density distribution along the $(x,0,0)$ axis for $Kn_s=0.002$, $P_s/P_b=220$. It can be seen that increasing L/D values gives smaller peaks. However, all L/D values (except $L/D=8$) give similar values as the Mach disk location is approached and for all L/D values (except $L/D=8.0$) the locations of the Mach disk in the secondary jet are very close to each other ($X_{M,secondary}/D\approx13$). This may due to the large P_s/P_b value used ($P_s/P_b=220$). When P_s/P_b is large, the position of the Mach disk X_M/D can be expected to be a large value. Consider the definition of the penetration Knudsen number in Equation (14), when X/D is large, θ becomes small and the interaction between the two jets is very weak at this location. Therefore, although the change of L/D may greatly affect the interaction of the two jets in the region when X/D is small, this change may not affect the location of the Mach disk in the secondary jet, where X/D is very large.

Figure 24 shows the density distribution along the $(x, 0, L/2)$ axis (symmetry axis of primary jet) for $Kn_s=0.002$, $P_s/P_b=220$, with different values of L/D. The plot shows that the primary jet is also affected by the interaction between the two jets, especially when L/D is small. When the interaction effects are stronger, due to the existence of the strong oblique shock waves, the jet is less likely to cross the symmetry plane, leading to larger velocities (from decreasing cross-sectional area). Thus, the location of the Mach disk in the primary jet moves further downstream.

Figure 25 shows the location of the Mach disk in the primary and secondary jets obtained from the DSMC results with comparison with Soga's experimental data.[19] Although some deviations can be observed, the DSMC results and experimental data, similar trends are exhibited.

Figure 26 shows the density distribution along the $(x,0,0)$ symmetry axis for $P_s/P_b=200$, $L/D=3.0$, with different values of Kn_s. The effects of Kn_s to the interaction region are shown. As expected, it can be seen that reducing Kn_s values increases the interaction between the two jets and hence, the curves have higher peaks. When Kn_s is very large ($Kn_s=0.02$), the flow is too rarefied and there is no Mach disk formed in the interaction region.

Figure 27 shows the density distribution along the $(x,0,0)$ symmetry axis for $Kn_s=0.005$, $L/D=3.0$ for different values of P_s/P_b. The effects of P_s/P_b to the interaction region are shown. Since the value of L/D is same, the location of the peak values is almost same (around $X/D\approx3$). As expected, reducing P_s/P_b strengthens the interaction between the secondary jet and the background gas. When P_s/P_b is small, stronger Mach disk is formed in the secondary jet and its location moves toward upstream. Different with the primary jets, in which the background gas cannot affect the expansion core, it can be seen that the existence of the background pressure significantly modifies the secondary jet flows. The reason may due to the relatively smaller density in the secondary jet, so that the flow in the secondary jet is more rarefied than the flow in the primary jets. Therefore, the can more easily penetrate into the secondary jet flow.

Since the secondary jet is very rarefied, it can be expected that the translational-rotational non-equilibrium effects are strong in the secondary jet. Figure 28 plots the translational and rotational temperature profiles along the $(x,0,0)$ symmetry axis for $Kn_s=0.002$, $P_s/P_b=220$ with different values of L/D. It can be found that when L/D is small, the interaction between the two jets leads to a strong secondary jet. Similar to a single under-expanded jet, large deviation between the two temperatures can be found in both fast expansion region and the region where Mach disk exists. However, large deviations between the translational and rotational temperatures are also found in the region close to the orifice plane, which may due to the low density in this region.

Figure 29 also plots the translational and rotational temperature profiles along the $(x,0,0)$ symmetry axis but for $Kn_s=0.005$, $L/D=3.0$ with different values of P_s/P_b. Since the increase of the background pressure P_b can greatly increase the density of the secondary jet (Figure 27), therefore, it can be found that the background gas helps to reduce the translational-rotational non-equilibrium effects in the secondary jet.

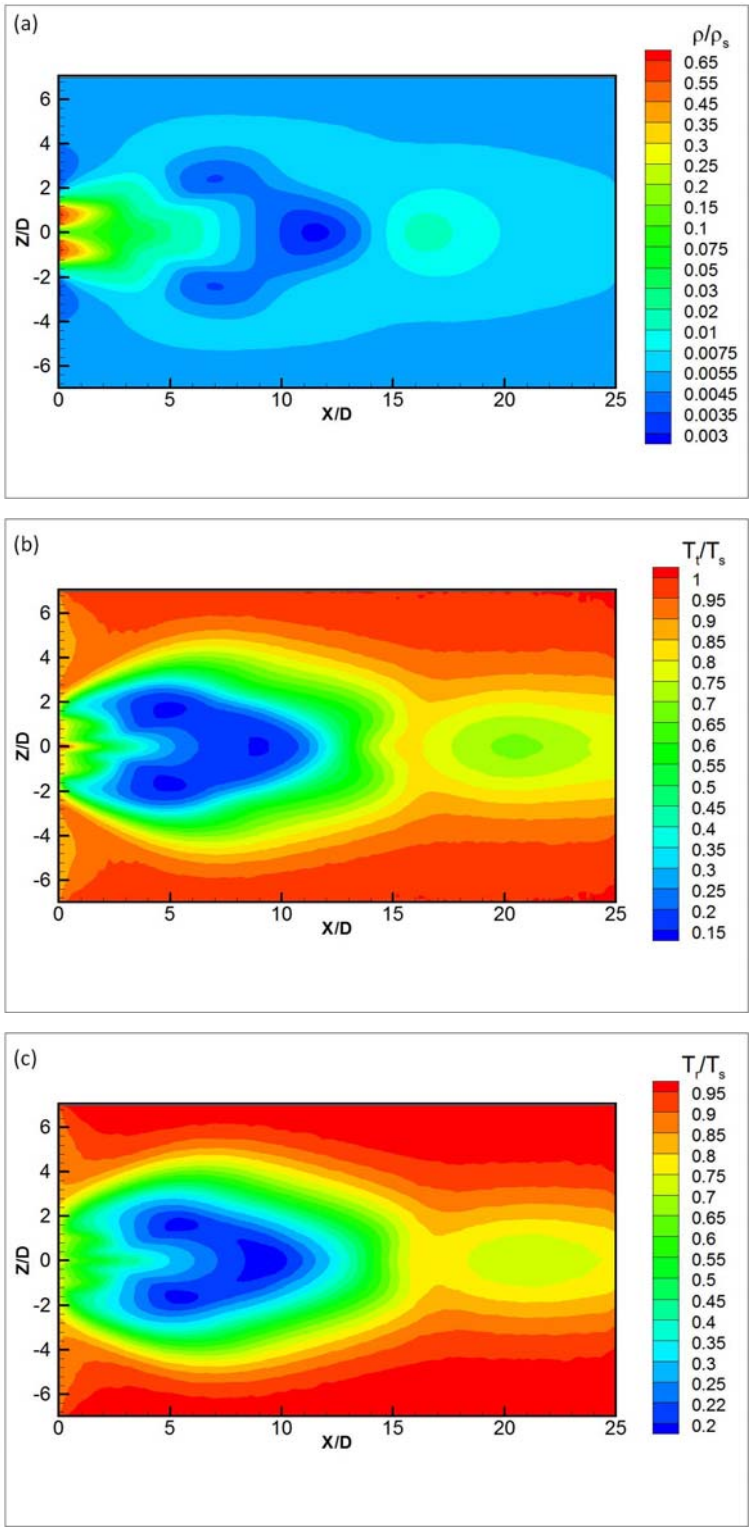

Figure 21. The (a) density; (b) translational temperature; and (c) rotational temperature contours in *y=0* plane for *L/D=1.5*, Kn_s*=0.002*, and P_s/P_b*=220*

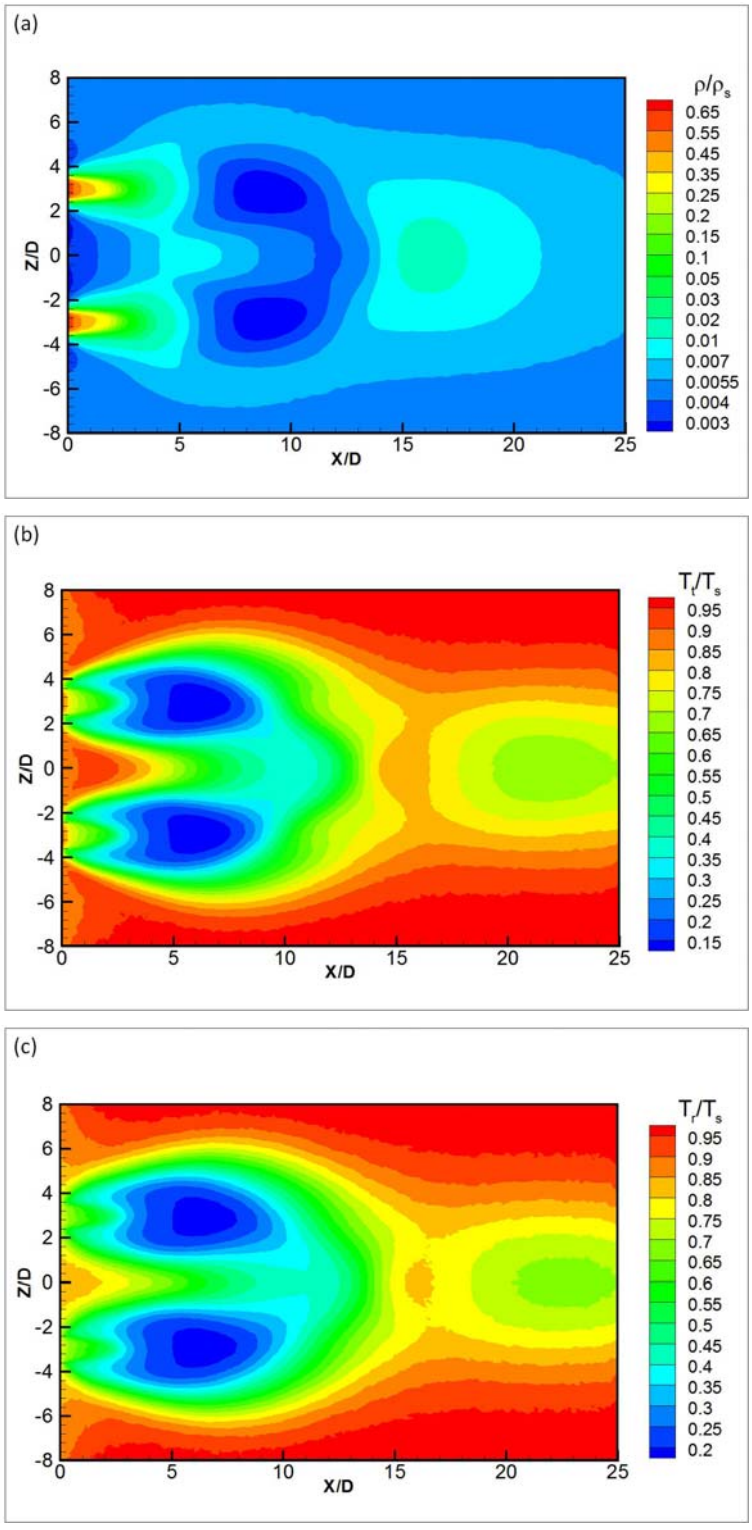

Figure 22. The (a) density; (b) translational temperature; and (c) rotational temperature contours in *y=0* plane for *L/D=6.0*, Kn_s*=0.002*, and P_s/P_b*=220*

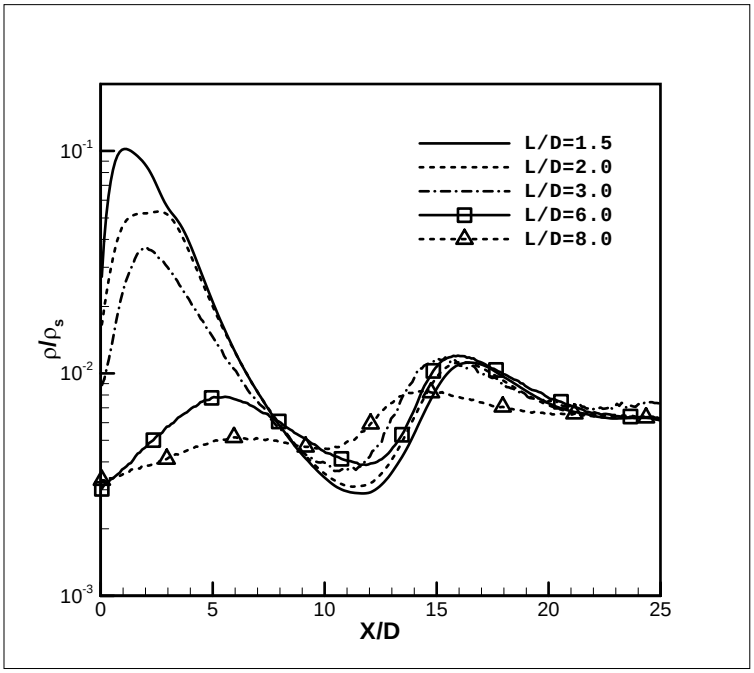

Figure 23. Density distributions along the *(x,0,0)* symmetry axis for Kn_s=0.002, P_s/P_b=220, with *L/D=1.5, 2.0, 4.0, 6.0,* and *8.0*.

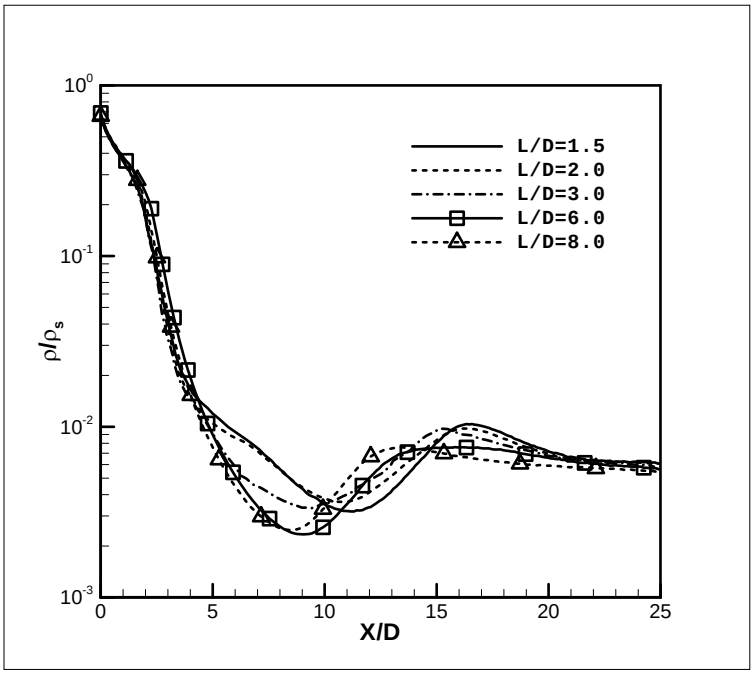

Figure 24. Density distributions along the *(x,0,L/2)* axis for Kn_s=0.002, P_s/P_b=220, with *L/D=1.5, 2.0, 4.0, 6.0,* and *8.0*.

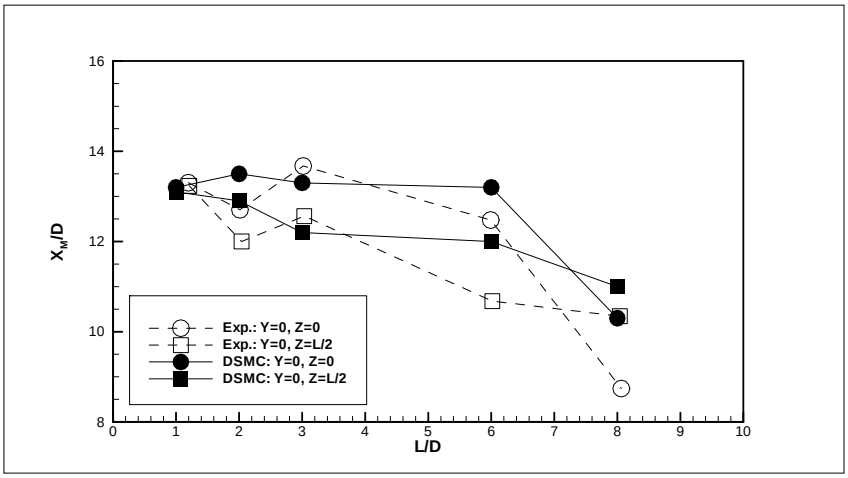

Figure 25. The location of Mach disk in the both of primary jet (*z=0*) and secondary jet (*z=L/2*) with the comparison with Soga's experimental data.[19]

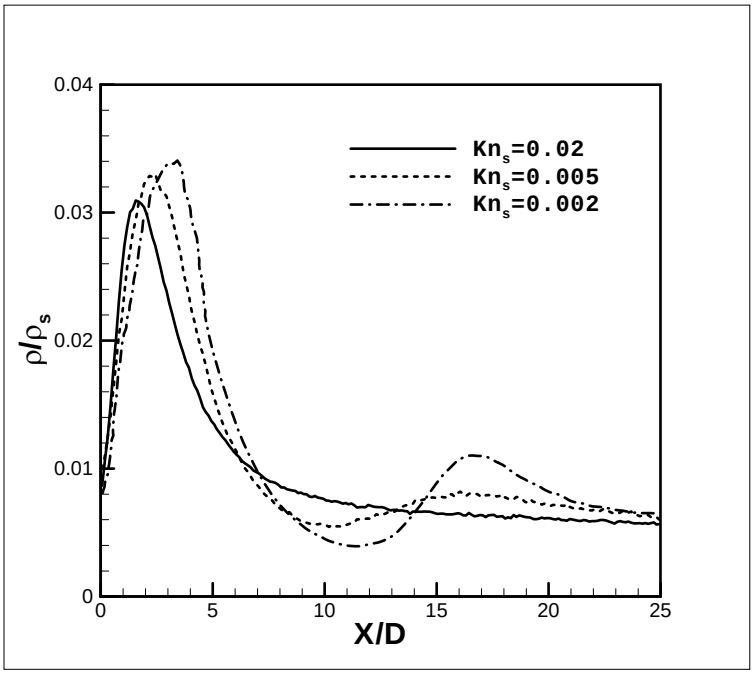

Figure 26. Density distributions along the *(x,0,0)* symmetry axis for P_s/P_b=200, L/D=3.0, with Kn_s=0.02, 0.005, and 0.002.

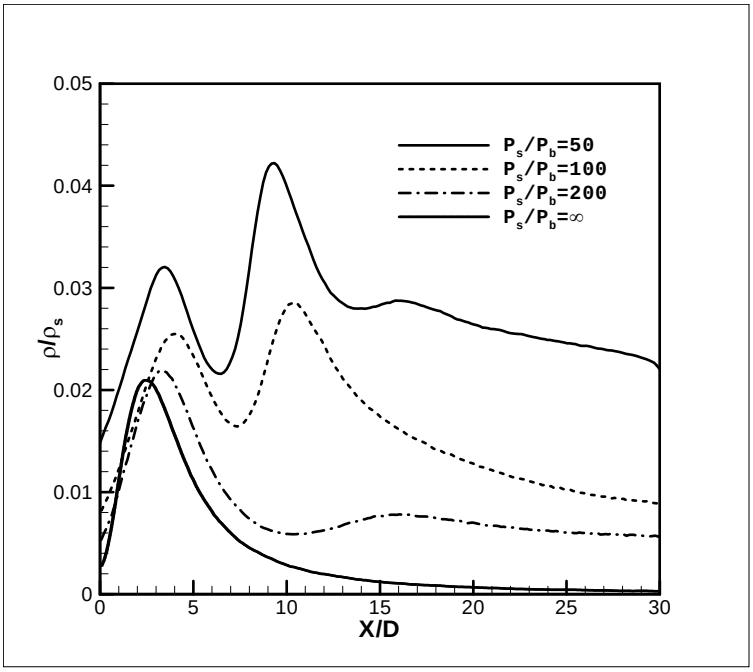

Figure 27. Density distributions along the (*x,0,0*) symmetry axis for Kn_s=0.005, L/D=3.0, with P_s/P_b=50, 100, 200, and ∞.

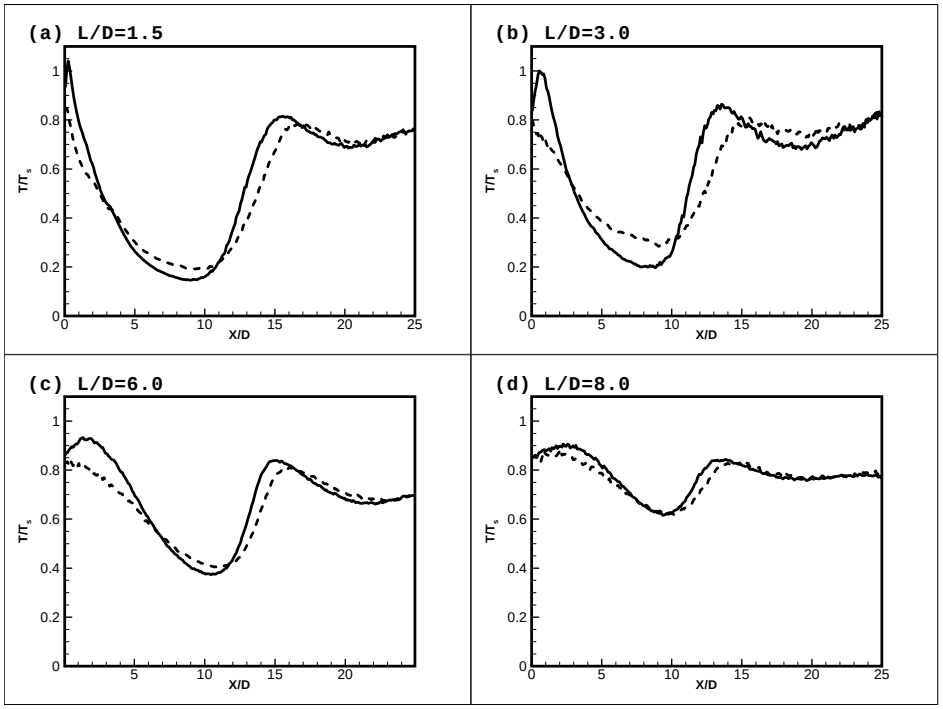

Figure 28. Translational Temperature (———) and rotational temperature (- - - - -) distributions along the (*x,0,0*) symmetry axis for Kn_s=0.002, P_s/P_b=220 with different values of L/D=3.0: (a) L/D=1.5; (b) L/D=3.0; (c) L/D=6.0; (d) L/D=8.0

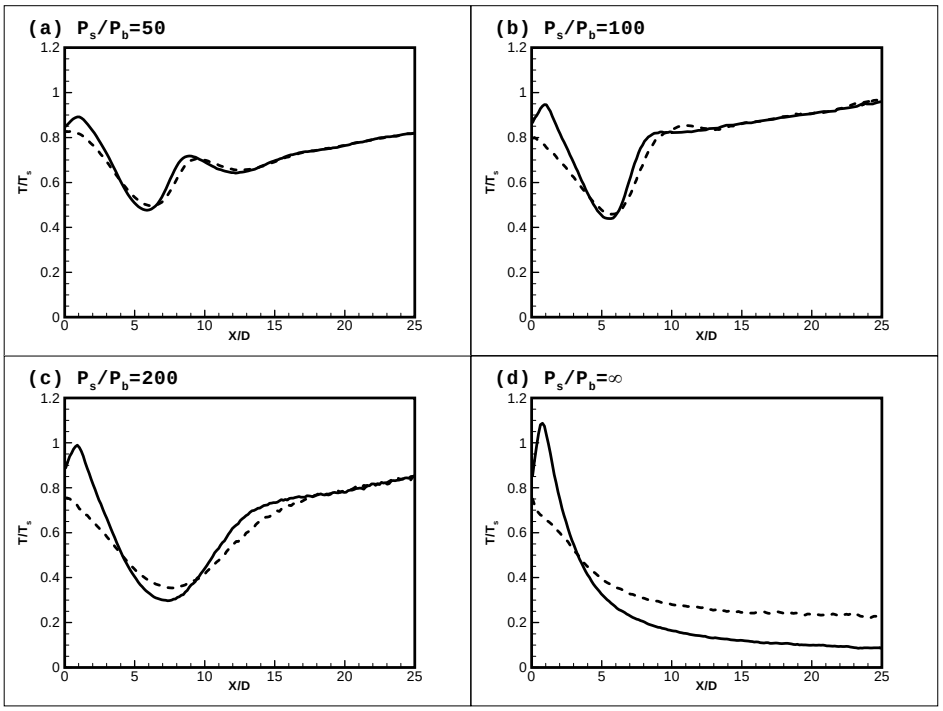

Figure 29. Translational Temperature (———) and rotational temperature (- - - - -) distributions along the (*x,0,0*) symmetry axis for Kn_s=0.005, L/D=3.0 with different values of P_s/P_b: (a) P_s/P_b=50; (b) P_s/P_b=100; (c) P_s/P_b=200; (d) $P_s/P_b \to \infty$.

IV. Conclusion

This paper reports the investigation of the physics of the dual interacting jets, for stagnation Knudsen number (Kn_s) within the range $0.002 \le Kn_s \le 0.02$, the separation between the jet orifices (L/D) in the range $1.5 \le L/D \le 8.0$, and stagnation-to-background pressure ratios (P_s/P_b) between *50* and values that approach infinity. The DSMC results compare well with experimental data. It was found that:

(1) Unlike the primary jets, in which the background gas cannot affect the expansion core, the existence of the background pressure significantly modifies the secondary jet flows.

(2) The value of L/D affects the locations of the Mach disk in both primary and secondary jets. But when P_s/P_b is relatively large (such as P_s/P_b=220) and L/D is relatively small ($L/D \le 6.0$), the separation distance L/D has only a mild effect on the location of the Mach disk in the secondary jet.

(3) The secondary jet is much more rarefied than the primary jet. Thermal non-equilibrium effects are significant in the secondary jet, especially in the vicinity of the orifice plate. The background gas helps to reduce the translational-rotational non-equilibrium effects in the secondary jet.

Acknowledgments

The authors would like to acknowledge TTC Technologies, Inc., for providing the computer development environment for the DSMC code and making the AEROFLO software available to them free-of-charge. Stony Brook University is also acknowledged for providing the parallel simulation environment.

References

[1]Li, W. and Ladeinde, F., "Simulation and Analysis of Rarefied Parallel Interacting Sonic Jets," AIAA-2006-1192.

[2]Li, W., Simulation and Analysis of Rarefied Parallel Interacting Sonic Jets, Master's thesis, Department of Mechanical Engineering, Stony Brook University, NY, 2004.

[3]J. Sahu, J., "Numerical Computations of Three Dimensional Jet Interaction Flow Fields," AIAA-94-3521.

[4]Houshang, B. E., Levine, J. and Kawasaki, A., "Numerical Investigation of Twin-Nozzle Rocket Plume Phenomenology," Journal of Propulsion and Power, Vol. 16, No. 2, 2000, pp. 178-186.

[5]Dagum, L. and Zhu, S. H. K., "DSMC Simulation of the Interaction Between Rarefied Free Jets," AIAA-93-2872.

[6]Zhu, S. H. K. and Dagum, L., "A Parametric Study of Rarefied Jet Interaction Using DSMC," AIAA-94-2046.

[7]Zhu, S. H. K. and Dagum, L., "Self-Similarity in Rarefied Jet Interactions - a DSMC Study," AIAA-95-2030.

[8]Koppenwallner, G., "Scaling Laws for Rarefied Plume Interaction with Application to Satellite Thrusters," Proceedings of the 14th International Symposium on Space Technology and Science, Tokyo, May 1984, pp. 505-512.

[9]Ketsdever, A. Selden, N., Gimelshein, S., Alexeenko, A., Vashchenkov, P., and Ivanov, M., "Plume Interactions of Multiple Jets Expanding into Vacuum: Experimental Investigation," AIAA-2004-1348.

[10]Pal, S., Dey, S., and Miebach, T., "Numerical Simulation of a Dual-Source Supersonic Plasma Jet Expansion Process: Continuum approach," Journal of Physics D: Applied Physics, Vol. 40, 2007, pp. 3128-3136.

[11]Schaepkens, M., Selezneva, S., Moeleker, P., and Iacovangelo, C. D., "High-Rate Deposition of Abrasion Resistant Coatings Using a Dual-Source Expanding Thermal Plasma Reactor," Journal of Vacuum Science & Technology A: Vacuum, Vol. 21, 2003, pp. 1266-1271.

[12]Autric, M., Lambert, L., and Itina, T., "Experimental and Theoretical Study of Dual-Crossed-Beam Pulsed Laser Deposition," Proceedings of SPIE, Vol. 4070, 2000, pp.252-261.

[13]Ladeinde, F., Cai, X., Alabi, K., Reba, R., Schlinker, R., and Simonich, J., "On the Connection Between Near- Field and Far- Field Solutions of High- Speed Jet Noise," AIAA-2008-0011.

[14]Ladeinde, F., Alabi, K., Colonius, T., Gudmundsson, K., Schlinker, R., and Reba, R., "An Integrated RANS- PSE- Wave Packet Tool for the Prediction of Subsonic and Supersonic Jet Noise," AIAA-2010-4021.

[15]Dankert, C. and Koppenwallner, G., "Experimental Study of Interaction Between Two Rarefied Free Jets," Rarefied Gas Dynamics: Proceeding of the 14th International Symposium on Rarefied Gas Dynamics, 1984, pp. 477-484.

[16]Cluass, J. S., Wright, B. R., and Bowie, G. E., "Twin Jet Noise Shielding for a Supersonic Cruise Vehicle," AIAA Paper 79-670.

[17]Seiner, J. M., Manning, J. C., and Pooton, M. K., "Dynamic Pressure Loads Associated with Twin Supersonic Plume Resonance," AIAA Paper 86-1539.

[18]Seiner, J. M., Manning, J. C., and Pooton, M. K., "Model and Full-Scale Study of Twin Supersonic Plume Resonance," AIAA Paper 87-0244.

[19]Soga, T., Takanishi, M. and Yasuhara, M., "Experimental Study of Interaction of Underexpanded Free Jets," Rarefied Gas Dynamics: Proceedings of the 14th International Symposium on Rarefied Gas Dynamics, July 1984, Tsukuba Science City, Japan, pp. 485-493.

[20]Niimi, T., Fujimoto, T., and Taoi, N., "Flow Fields of Interacting Parallel Supersonic Free Jets," JSME International Journal, Series B, Vol. 39, No. 1, 1996, pp. 95-100

[21]Ladeinde, F., Cai, X., Li, W., and Agarwal, R., "A Unified Computational Methodology for Rarefied and Continuum Flow Regimes", AIAA-2004-1178.

[22]Ladeinde, F., Cai, X., and Agarwal, R., "On the Stability of High-Order Continuum (HOC) Equation for Hybrid HOC/DSMC Solvers," Proceedings of the 24th International Symposium on Rarefied Gas Dynamics, 2004, pp. 535-540.

[23]Wu, J. S., Tseng, K. C., and Wu, F. Y., "Parallel Three-Dimensional DSMC Method Using Mesh Refinement and Variable Time-Step Scheme," Computer Physical Communications, Vol. 162, 2004, pp. 166-187

[24]Ikegawa, M., and Kobayashi, J., "Development of a Rare+1X Rarefied Flow Simulator Using the Direct Simulation Monte Carlo Method," JSME International Journal, Series 2, Vol. 33, No. 3, 1990, pp. 463-467.

[25]Nance, P. R., Hash, D. B., and Hassan, H. A., "Role of Boundary Conditions in Monte Carlo Simulation of Microelectromechanical System," Journal of Thermalphysics and Heat Transfer, Technical Notes, Vol. 12, No. 3, 1998, pp. 447-449.

[26]Wu, J.-S., Lee, F., and Wong, S.-C., "Pressure Boundary Treatment in Micromechanical Devices Using the Direct Simulation Monte Carlo Method," JSME International Journal, Series 2, Vol. 44, 2001, pp. 439-450 (2001).

[27]Wu, J.-S., Chou, S.-Y., Lee, U.-M., Shao, Y.-L., and Lian, Y.-Y., "Parallel DSMC Simulation of a Single Under-Expanded Free Orifice Jet from Transition to Near-Continuum Regime," Journal of Fluids Engineering, Vol. 127, 2005, pp. 1161-1170.

[28]Li, W. and Ladeinde, F., "Analysis of Single Under-Expanded Jets in Rarefied and Near-Continuum Regimes," AIAA Journal (To be Submitted).

[29]Usami, M., and Teshima, K., "Three Dimensional DSMC Calculation of Interacting Flowfield in Two Parallel Underexpanded Jets," Rarefied Gas Dynamics: Proceeding of the 21th International Symposium on Rarefied Gas Dynamics, 1999, pp.569-576

[30]Bird, G. A., Molecular Gas Dynamics and the Direct Simulation of Gas Flows. 1st Ed., Oxford Univ. Press, Oxford, 1994.

[31]Oran, E. S., Oh, C. K., and Cybyk, B. Z., "Direct Simulation Monte Carlo: Recent Advances and Applications," Annual Review of Fluid Mechanics, Vol. 30, 1998, pp. 403-441.

[32]Wysong, I. J., and Wadsworth, D. C., "Assessment of Direct Simulation Monte Carlo Phenomenological Rotational Relaxation model," Physics of Fluids, Vol. 10, No. 11, 1998, pp. 2983-2994.

[33]Cai, C., Boyd, I. D., Fan, J., and Candler, G. V., "Direct Simulation Methods for Low-Speed Micro-Channel Flows," AIAA Paper No. 99-3801.

[34]Marrone, P. V., "Temperature and Density Measurements in Free Jets and Shock Waves," Physics of Fluids, Vol. 10, 1967, pp. 521--538.

[35]Mori, H., Niimi, T., Akiyama, I., Tsuzuki, T., "Experimental Detection of Rotational Non-Boltzmann Distribution in Supersonic Free Molecular Nitrogen Flows," Physics of Fluids, Vol. 17, 2005, pp. 117103.

[36]Anonymous, AEROFLO's User Manual, TTC Technologies, Inc., 2004.

[37]Albini, F. A., "Approximate Computation of Underexpanded Jet Structure," AIAA Journal, Vol. 3, 1965, pp. 1535-1537.

[38]Hubbard, E. W., "Approximate Calculation of Highly Underexpanded Jets," AIAA Journal, Vol. 4, 1966, pp. 1877-1879.

[39]Boyton, "Highly Underexpanded Jet Structure: Exact and Approximate Calculations," AIAA Journal, Vol. 8, 1967, pp. 1703-1704.

[40]Young, W. S., "Derivation of the Free-Jet Mach-Disk Location Using the Entropy-Balance Principle," Physics of Fluids, Vol. 18, No. 11, 1975, pp. 1421-1425.

[41]Muntz, E. P., Hamel, B. B. and Maguire, B. L., "Some Characteristics of Exhaust Plume Rarefaction," AIAA J., Vol 8, No. 9 (1970), pp. 1651-1658.

[42]Ashkenas, H. and Sherman, F. S., "The Structure and Utilization of Supersonic Free Jets in Low Density Wind Tunnels," Rarefied Gas Dynamics, Fourth Symposium, Vol. II, Academic Press, New York, 1966, pp. 311-330.

[43]Crist, S., Sherman, F. S., and Glass, D. R., "Study of Highly Under-Expanded Sonic Jet," AIAA Journal, Vol. 4, 1966, pp. 68-71.

[44]Gldalevich, E., Boxman, R. L., and Goldsmith, S., "Theory and Modeling of the Interaction of Two Parallel Supersonic Plasma Jets," J. Phys. D: Appl. Phys., Vol. 31, pp. 304-311, 1998.